SPITZER IRAC PHOTOMETRY OF M, L, AND T DWARFS

BRIAN M. PATTEN,[1] JOHN R. STAUFFER,[2] ADAM BURROWS,[3] MASSIMO MARENGO,[1] JOSEPH L. HORA,[1]
KEVIN L. LUHMAN,[1,4] SARAH M. SONNETT,[1,5] TODD J. HENRY,[6] DEEPAK RAGHAVAN,[6]
S. THOMAS MEGEATH,[1] JAMES LIEBERT,[3] AND GIOVANNI G. FAZIO[1]

ABSTRACT

We present the results of a program to acquire photometry for 86 late M, L, and T dwarfs using the Infrared Array Camera (IRAC) on the *Spitzer Space Telescope*. We examine the behavior of these cool dwarfs in various color-color and color-magnitude diagrams composed of near-IR and IRAC data. The T dwarfs exhibit the most distinctive positions in these diagrams. In $M_{5.8}$ versus [5.8]−[8.0], the IRAC data for T dwarfs are not monotonic in either magnitude or color, giving the clearest indication yet that the T dwarfs are not a one-parameter family in $T_{\rm eff}$. Because metallicity does not vary enough in the solar neighborhood to act as the second parameter, the most likely candidate then is *gravity*, which in turn translates to *mass*. Among objects with similar spectral type, the range of mass suggested by our sample is about a factor of 5 ($\sim 70 M_J$ to $\sim 15 M_J$), with the less massive objects making up the younger members of the sample. We also find the IRAC 4.5 μm fluxes to be lower than expected, from which we infer a stronger CO fundamental band at ~ 4.67 μm. This suggests that equilibrium CH_4/CO chemistry underestimates the abundance of CO in T dwarf atmospheres, confirming earlier results based on *M*-band observations from the ground. In combining IRAC photometry with near-IR *JHK* photometry and parallax data, we find the combination of K_s, IRAC 3.6 μm, and 4.5 μm bands to provide the best color-color discrimination for a wide range of M, L, and T dwarfs. Also noteworthy is the M_{K_s} versus K_s−[4.5] relation, which shows a smooth progression over spectral type, and splits the M, L, and T types cleanly.

Subject headings: infrared: stars — stars: fundamental parameters — stars: late-type — stars: low-mass, brown dwarfs

Online material: color figures

1. INTRODUCTION

The study of low-mass dwarfs has progressed enormously in the last decade: from the strictly theoretical beginnings for objects of substellar mass (e.g., Kumar 1963; Grossman 1970; Nelson et al. 1985) to the actual discovery in the late-1980s and mid-1990s of objects in two new spectral classes later than M (Becklin & Zuckerman 1988; Nakajima et al. 1995). As a result of a large amount of observational effort over the past decade, the temperature sequence of dwarfs has been extended down to $T \sim 700$ K (Golimowski et al. 2004a). Several hundred L dwarfs and several dozen T dwarfs have now been identified, leading to well-defined L and T spectral sequences (Kirkpatrick 2005) and to a large body of accurate photometry and quantitative spectroscopy to characterize those spectral types (Leggett et al. 2001, 2002; Basri et al. 2000; Reid et al. 2002). Also of importance is the fact that other groups have been able to obtain accurate trigonometric parallaxes for a large number of these very cool dwarfs (e.g., Dahn et al. 2002; Tinney et al. 2003; Vrba et al. 2004) and to obtain dynamical masses for a significant sample of stars (e.g., Henry & McCarthy 1993; Henry et al. 1999; Lane et al. 2001; Zapatero Osorio et al. 2004; Bouy et al. 2004; Close et al. 2005).

The observational progress was accompanied by an equally dramatic evolution in the sophistication of the theoretical models of cool dwarfs. The improved observational data spurred theoretical model efforts such as Allard et al. (1994) and Brett (1995), who were able to incorporate much more extensive molecular line lists and thus improve the fit to observations and extend the model spectra further into the infrared. The model atmospheres have since rapidly evolved, incorporating ever-larger molecular line lists, dust formation and dust settling, and improved treatment of pressure broadening, particularly for the alkali lines that dominate the optical and near-IR spectra of the L dwarfs. More recently, the models have begun to take into account nonequilibrium chemistry (e.g., Noll et al. 1997; Saumon et al. 2000, 2003, 2006; Burrows et al. 2000; Ackerman & Marley 2001; Allard et al. 2001; Lodders & Fegley 2002; Marley et al. 2002; Tsuji 2002).

While much of the work on substellar mass objects to date has been carried out in the optical and near-IR, there is great potential to gain even more insight into brown dwarf atmospheres by extending observations into the mid-IR regime. The advantages include the peaking of the spectral energy distribution for L and T dwarfs between 1 and 4 μm, and the presence of prominent molecular features such as CH_4, H_2O, and NH_3 (e.g., Burrows et al. 1997, 2001). Ground-based infrared observations are hampered longward of the *K* band by telluric atmospheric lines, such as OH and H_2O, making the atmosphere increasingly opaque at these wavelengths. Thermal emission of the atmosphere and telescope structure also causes very high backgrounds for ground-based observations longward of the *K* band. Thus, space-based instruments with sensitivity in the mid-infrared are required for the study of substellar mass objects in this wavelength regime. It was in this context that the IRAC Guaranteed Time Observer (GTO)

[1] Harvard-Smithsonian Center for Astrophysics, 60 Garden Street, Cambridge, MA 02138-1516; bpatten@cfa.harvard.edu.

[2] *Spitzer* Science Center, Mail Stop 314-6, California Institute of Technology, Pasadena, CA 91125.

[3] Department of Astronomy, The University of Arizona, Tucson, AZ 85721.

[4] Department of Astronomy and Astrophysics, Pennsylvania State University, 525 Davey Lab, University Park, PA 16802.

[5] Department of Physics and Astronomy, College of Charleston, 101 Hollings Science Center, 58 Coming Street, Charleston, SC 29424.

[6] Department of Physics and Astronomy, Georgia State University, Atlanta, GA 30302-4106.

team decided that it would be important to obtain accurate mid-IR fluxes for a representative sample of M, L, and T dwarfs when the *Spitzer Space Telescope* was launched.

We present in this paper the results of this survey. In § 2 we describe the sample selection of M, L, and T dwarfs and their basic properties. In § 3 we summarize the observing strategy used with *Spitzer* IRAC, and the subsequent data reduction and extraction of the IRAC photometry. In § 4 we present the basic color-color and color-magnitude diagrams for both IRAC and near-IR *JHK* photometry and discuss trending with color and spectral type. Finally, in § 5, we conclude with a few tentative interpretations of the observations.

2. THE SAMPLE

The targets in our program were selected from the literature. Because the GTO program target selection was frozen a year prior to the *Spitzer* launch on 2003 August 25, our selection was limited to those objects cataloged at that time. The primary consideration that governed our selection process was whether or not the target had a measured trigonometric parallax. The secondary constraints on our selections were: (1) we wanted the sources to be relatively bright in order to ensure good signal-to-noise ratio (S/N) on the photometry, given our observing strategy (see § 3), since these objects would represent the fiducial sample for other science programs; (2) the targets needed to have well-determined spectral types because of the desire to have representatives of all spectral subtype bins from late M through T types; (3) the targets needed to be located in relatively uncrowded fields; and (4) the targets should not be close binaries (separations of $\leq 6''$, or about 5 IRAC pixels). While we tried to avoid including binaries in our sample, the information available in the literature was/is quite incomplete, so some now-known binaries were included in our program. Other objects may be binaries, but are currently not known as such. Given that dwarfs in the L7–T2 spectral type range have been found to have a high binary fraction (e.g., Burgasser et al. 2006b), it seems inevitable that more objects in our sample will turn out to be binaries than we have currently noted.

The basic properties of the objects in our sample are summarized in Table 1. We provide here position, nomenclature, parallax (if available), spectral type, and near-IR photometry. Some target names are abbreviated from their official forms. Objects from the Deep Near Infrared Survey of the Southern Sky (DENIS), Two Micron All Sky Survey (2MASS), and Sloan Digital Sky Survey (SDSS) have had their survey acronyms shortened to three characters—DEN, 2MA, and SDS, respectively—followed by the first four digits of right ascension and then the first four digits of the declination. For the *JHK$_s$* photometry, we use data from 2MASS primarily in order to maintain consistency. However, in those cases where the 2MASS errors are large ($\gtrsim 0.20$ mag) or other flags in the database (e.g., blending, contamination, confusion) suggest questionable photometric reliability, we tabulate photometry from the literature (see references in Table 1). Because the near-IR photometry for low-mass dwarfs is strongly system dependent (particularly for T dwarfs), we have chosen to rely on MKO-system photometry when reliable 2MASS photometry is not available. We make this choice because there are well-documented transformations between these two systems (Stephens & Leggett 2004) as well as a wealth of MKO-system photometry for low-mass brown dwarfs available in the literature (see additional discussion in § 4.1.2). For two T dwarfs in our sample (SDS 1624+0029 and 2MA 1237+6526), we acquired new *JHK$_s$* photometry with the Peters Automated Infrared Imaging Telescope (PAIRITEL) facility on Mt. Hopkins (telescope and instrument formerly used for the 2MASS project; see Bloom et al. [2006] for

additional details). This photometry was calibrated to the 2MASS system using local comparison stars in each field of view. Because the T dwarfs are intrinsically faint in the optical, it is difficult to classify these objects using the same criteria/features that work for the brighter L dwarfs. For the spectral types in Table 1, we have chosen to quote optical types for the M and L dwarfs while, for the T dwarfs, infrared types are used. Near-IR classification systems take advantage of the peak of the spectral energy distribution being located in the infrared for T dwarfs and a wealth of molecular features in this wavelength regime. The unified near-IR classification system for T dwarfs (Burgasser et al. 2006a) is compatible with optical classification systems (e.g., Kirkpatrick et al. 1999, 2000) at type L8, creating a smooth continuum of types from M through T. It is worth noting, however, that for the L dwarfs, the optical and near-IR spectral types can be quite different, as they probe different optical depths in each wavelength regime (see the discussion in Knapp et al. [2004] and Kirkpatrick [2005]).

In addition to our primary MLT sample, unsaturated photometry was secured for a number of late M dwarfs from a related GTO program (PID 33, "A Search for Companions around Stars within Five Parsecs"). These include GJ 1002, LHS 288, GJ 412B, GJ 1111, LHS 292, SO 0253+1652, and LP 944−020. Archival data from an unpublished *Spitzer* Early Release Observation yielded photometry for the T dwarf binary ϵ Indi BC, which is also presented in Table 1. Although GJ 229B was included in the nominal MLT GTO program, it was lost in the glare from GJ 229, so IRAC photometry could not be secured for this object. In total, supporting data for 86 objects for which we were able to secure IRAC photometry are presented in Table 1.

2.1. *Comments on Specific Sources*

As of the writing of this paper, the following objects have been determined to be binaries, unresolved or blended at the IRAC plate scale of $\sim 1\rlap{.}{''}2$ pixel^{-1}: GJ 1001BC, SDS 0423−0414, 2MA 0746+2000, GJ 337CD, SDS 0926+5847, SDS 1021−0304, Kelu-1, 2MA 1225−2739, 2MA 1534−2952, 2MA 1553+1532, and 2MA 1728+3948 (Reid et al. 2001; Burgasser et al. 2003b, 2005a, 2005b, 2006b; Gizis et al. 2003; Bouy et al. 2004; Golimowski et al. 2004b; Vrba et al. 2004; Liu & Leggett 2005). The following objects have been noted to have spectral peculiarities—unusually weak metal lines for their subtype, emission lines in their spectra, or unusual colors—suggesting that some of these may be metal-poor subdwarfs; however, multiplicity may also play a role: 2MA 0559−1404, 2MA 0937+2931, 2MA 1047+2124, SDS 1110+0116, 2MA 1217−0311, 2MA 1237+6526, and SDS 1624+0029 (Burgasser et al. 2002, 2003a; Tinney et al. 2003; Golimowski et al. 2004a).

2MA 0532+8246.—This object, the first identified late-type L subdwarf (Burgasser et al. 2003b), has been confirmed as such in Reiners & Basri (2006).

BRI 0021−0214.—Photometric variability has been reported in the *I* band with a full amplitude of about 0.05 mag and possible periods of about 0.2 and 0.83 days (Martín et al. 2001). However, its large $v \sin i$ of ~ 34–42 km s^{-1} (Tinney & Reid 1998; Mohanty & Basri 2003), if true, would indicate a rotation period significantly less than 0.8 days.

DENIS 0255−4700.—Has a very high $v \sin i$ of 40 km s^{-1} (Mohanty & Basri 2003). A suggestion of photometric variability could be explained in part by rotational modulation (Koen 2005).

LP 944−020.—Listed as a member of the Castor moving group by Ribas (2003); thus, its age is ~ 300–500 Myr. Tinney (1998) gave an age of 475–650 Myr for this star, based on the detection of lithium and the star's L_{bol}.

TABLE 1
The Sample of Late-type M, L, and T Dwarfs: Basic Data

Name	R.A. (J2000.0)	Decl. (J2000.0)	Spectral Type[a]	Spectral Type Ref.	π (error) (arcsec)	π Ref.	J (error)	H (error)	K_s (error)	JHK Ref.	Photometric System
GJ 1001A........................	00 04 36.4	−40 44 03	M3.5	1	. . .	. . .	8.60 (0.01)	8.04 (0.03)	7.74 (0.04)	1	2MA
GJ 1093.........................	06 59 28.9	+19 20 53	M5.0	2	0.12880 (0.00350)	1	9.16 (0.02)	8.55 (0.02)	8.23 (0.02)	1	2MA
GJ 1156.........................	12 18 59.5	+11 07 33	M5.0	2	0.15290 (0.00300)	1	8.53 (0.03)	7.88 (0.03)	7.57 (0.03)	1	2MA
GJ 1002.........................	00 06 43.4	−07 32 19	M5.5	2	0.21300 (0.00360)	1	8.32 (0.02)	7.79 (0.03)	7.44 (0.02)	1	2MA
LHS 288........................	10 44 21.3	−61 12 35	M5.5	3	0.22250 (0.01130)	1	8.49 (0.01)	8.05 (0.04)	7.73 (0.02)	1	2MA
GJ 412B	11 05 30.3	+43 31 17	M5.5	2	0.20694 (0.00119)	2	8.74 (0.03)	8.18 (0.02)	7.84 (0.03)	1	2MA
GJ 1111	08 29 49.5	+26 46 32	M6.5	4	0.27580 (0.00300)	1	8.24 (0.02)	7.62 (0.02)	7.26 (0.02)	1	2MA
LHS 292........................	10 48 12.8	−11 20 11	M6.5	2	0.22030 (0.00360)	1	8.86 (0.02)	8.26 (0.04)	7.93 (0.03)	1	2MA
SO 0253+1652................	02 53 00.5	+16 52 58	M7.0	5	0.26800 (0.03700)	3	8.39 (0.03)	7.88 (0.04)	7.59 (0.05)	1	2MA
LHS 3003......................	14 56 38.4	−28 09 48	M7.0	6	0.15630 (0.00300)	1	9.97 (0.03)	9.32 (0.02)	8.93 (0.03)	1	2MA
GJ 644C	16 55 35.3	−08 23 40	M7.0	4	0.15542 (0.00133)	4	9.78 (0.03)	9.20 (0.02)	8.82 (0.02)	1	2MA
LHS 132........................	01 02 51.2	−37 37 45	M8.0:	7	. . .	. . .	11.13 (0.02)	10.48 (0.02)	10.07 (0.02)	1	2MA
LHS 2021......................	08 30 32.7	+09 47 14	M8.0	5	. . .	. . .	11.89 (0.02)	11.17 (0.02)	10.76 (0.02)	1	2MA
GJ 752B	19 16 57.7	+05 09 00	M8.0	4	0.17010 (0.00080)	5	9.91 (0.03)	9.23 (0.03)	8.77 (0.02)	1	2MA
2MA 1835+3259	18 35 37.9	+32 59 54	M8.5	8	0.17650 (0.00050)	6	10.27 (0.02)	9.62 (0.02)	9.17 (0.02)	1	2MA
LP 944−020	03 39 35.2	−35 25 44	M9.0	9	0.20140 (0.00420)	7	10.73 (0.02)	10.02 (0.02)	9.55 (0.02)	1	2MA
LHS 2065......................	08 53 36.1	−03 29 30	M9.0	4	0.11730 (0.00150)	1	11.21 (0.03)	10.47 (0.03)	9.94 (0.03)	1	2MA
LHS 2924......................	14 28 42.0	+33 10 36	M9.0	6	0.09080 (0.00130)	8	11.99 (0.02)	11.23 (0.03)	10.74 (0.03)	1	2MA
DEN 0021−4244.............	00 21 05.8	−42 44 49	M9.5	10	. . .	. . .	13.52 (0.03)	12.81 (0.03)	12.30 (0.03)	1	2MA
BRI 0021−0214	00 24 24.6	−01 58 20	M9.5	1	0.08660 (0.00400)	8	11.99 (0.04)	11.08 (0.02)	10.54 (0.02)	1	2MA
2MA 1204+3212	12 04 30.4	+32 13 00	L0.0	11	. . .	. . .	13.82 (0.04)	13.09 (0.04)	12.52 (0.03)	1	2MA
2MA 0320−0446.............	03 20 28.4	−04 46 36	L0.5(IR)	12	. . .	. . .	13.26 (0.02)	12.54 (0.02)	12.13 (0.03)	1	2MA
2MA 0451−3402.............	04 51 00.9	−34 02 15	L0.5	10	. . .	. . .	13.54 (0.02)	12.83 (0.02)	12.29 (0.03)	1	2MA
2MA 0746+2000AB[b]	07 46 42.5	+20 00 32	L0.5	13	0.08190 (0.00030)	8	11.76 (0.02)	11.01 (0.02)	10.47 (0.02)	1	2MA
2MA 1300+1912	13 00 42.6	+19 12 35	L1.0	14	. . .	. . .	12.72 (0.02)	12.08 (0.02)	11.62 (0.02)	1	2MA
2MA 1439+1929	14 39 28.4	+19 29 15	L1.0	15	0.06960 (0.00050)	8	12.76 (0.02)	12.04 (0.02)	11.55 (0.02)	1	2MA
2MA 1555−0956.............	15 55 15.7	−09 56 06	L1.0	16	. . .	. . .	12.56 (0.02)	11.98 (0.02)	11.44 (0.03)	1	2MA
2MA 1645−1319.............	16 45 22.1	−13 19 52	L1.5	16	. . .	. . .	12.45 (0.03)	11.69 (0.02)	11.15 (0.03)	1	2MA
2MA 1017+1308	10 17 07.5	+13 08 40	L2.0:	11	. . .	. . .	14.10 (0.02)	13.28 (0.03)	12.71 (0.02)	1	2MA
2MA 1155−3727.............	11 55 39.5	−37 27 35	L2.0	16	. . .	. . .	12.81 (0.02)	12.04 (0.03)	11.46 (0.02)	1	2MA
Kelu-1[b]	13 05 40.2	−25 41 06	L2.0	15	0.05360 (0.00200)	8	13.41 (0.03)	12.39 (0.03)	11.75 (0.03)	1	2MA
DEN 1058−1548.............	10 58 47.9	−15 48 17	L3.0	15	0.05770 (0.00100)	8	14.16 (0.04)	13.23 (0.03)	12.53 (0.03)	1	2MA
2MA 1506+1321	15 06 54.4	+13 21 06	L3.0	14	. . .	. . .	13.37 (0.02)	12.38 (0.03)	11.74 (0.02)	1	2MA
2MA 1721+3344	17 21 03.9	+33 44 16	L3.0	11	. . .	. . .	13.63 (0.02)	12.95 (0.03)	12.49 (0.02)	1	2MA
SDS 2028+0052..............	20 28 20.4	+00 52 27	L3.0	17	. . .	. . .	14.30 (0.04)	13.38 (0.03)	12.79 (0.03)	1	2MA
2MA 2104−1037.............	21 04 14.9	−10 37 37	L3.0	11	. . .	. . .	13.84 (0.03)	12.98 (0.03)	12.37 (0.02)	1	2MA
2MA 0036+1821	00 36 15.9	+18 21 10	L3.5	13	0.11420 (0.00080)	8	12.32 (0.03)	11.63 (0.03)	11.03 (0.03)	3	MKO
DEN 1539−0520.............	15 39 41.9	−05 20 43	L4.0:	18	. . .	. . .	13.92 (0.03)	13.06 (0.03)	12.58 (0.03)	1	2MA
2MA 0141+1804	01 41 03.2	+18 04 50	L4.5(IR)	12	. . .	. . .	13.88 (0.03)	13.03 (0.03)	12.49 (0.03)	1	2MA
2MA 0652+4710	06 52 30.7	+47 10 35	L4.5	11	. . .	. . .	13.51 (0.02)	12.38 (0.02)	11.69 (0.02)	1	2MA
2MA 2224−0158.............	22 24 43.8	−01 58 52	L4.5	19	0.08810 (0.00110)	8	13.89 (0.03)	12.84 (0.03)	11.98 (0.03)	4	MKO
GJ 1001BC[b]...................	00 04 34.9	−40 44 06	L5.0	20	0.10470 (0.01140)	1	13.11 (0.02)	12.06 (0.03)	11.40 (0.03)	1	2MA
SDS 0539−0059..............	05 39 52.0	−00 59 02	L5.0	21	0.07612 (0.00217)	9	14.03 (0.03)	13.10 (0.03)	12.53 (0.02)	1	2MA
2MA 0835−0819.............	08 35 42.6	−08 19 24	L5.0	11	. . .	. . .	13.17 (0.02)	11.94 (0.02)	11.14 (0.02)	1	2MA
2MA 0908+5032	09 08 38.0	+50 32 09	L5.0	11	. . .	. . .	14.40 (0.03)	13.54 (0.03)	12.89 (0.03)	4	MKO
2MA 1507−1627.............	15 07 47.6	−16 27 38	L5.0	13	0.13640 (0.00060)	8	12.70 (0.03)	11.80 (0.03)	11.29 (0.03)	3	MKO
SDS 1331−0116..............	13 31 48.9	−01 16 50	L6.0	17	. . .	. . .	15.32 (0.03)	14.65 (0.03)	14.07 (0.03)	4	MKO
2MA 1515+4847	15 15 00.8	+48 47 42	L6.0(IR)	12	. . .	. . .	14.11 (0.03)	13.10 (0.03)	12.50 (0.02)	1	2MA
2MA 0717+5705	07 17 16.3	+57 05 43	L6.5(IR)	12	. . .	. . .	14.64 (0.03)	13.59 (0.03)	12.95 (0.03)	1	2MA
2MA 1526+2043	15 26 14.1	+20 43 41	L7.0	19	. . .	. . .	15.59 (0.06)	14.50 (0.04)	13.92 (0.05)	1	2MA
2MA 1728+3948[b]...........	17 28 11.5	+39 48 59	L7.0	19	0.04149 (0.00326)	9	15.99 (0.08)	14.76 (0.07)	13.91 (0.05)	1	2MA
2MA 0825+2115.............	08 25 19.6	+21 15 52	L7.5	19	0.09381 (0.00100)	8	14.89 (0.03)	13.81 (0.03)	12.93 (0.03)	3	MKO
DEN 0255−4700..............	02 55 03.6	−47 00 51	L8.0	18	. . .	. . .	13.25 (0.03)	12.20 (0.02)	11.56 (0.02)	1	2MA
SDS 0857+5708..............	08 57 58.5	+57 08 51	L8.0	24	. . .	. . .	14.80 (0.03)	13.80 (0.03)	12.94 (0.03)	3	MKO
GJ 337CD[b]....................	09 12 14.5	+14 59 40	L8.0	23	0.04880 (0.00092)	8	15.51 (0.08)	14.62 (0.08)	14.04 (0.06)	1	2MA
2MA 1632+1904	16 32 29.1	+19 04 41	L8.0	15	0.06560 (0.00210)	8	15.77 (0.03)	14.68 (0.03)	13.97 (0.03)	3	MKO
2MA 0532+8246	05 32 53.5	+82 46 46	sdL	22	. . .	. . .	15.18 (0.06)	14.90 (0.09)	14.92 (0.15)	1	2MA
SDS 0423−0414[b]	04 23 48.6	−04 14 04	T0.0	25	0.06593 (0.00170)	9	14.30 (0.03)	13.51 (0.03)	12.96 (0.03)	3	MKO
SDS 0151+1244..............	01 51 41.7	+12 44 30	T0.5	25	0.04673 (0.00337)	9	16.25 (0.05)	15.54 (0.05)	15.18 (0.05)	3	MKO
SDS 0837−0000..............	08 37 17.2	−00 00 18	T1.0	25	0.03370 (0.01345)	9	16.90 (0.05)	16.21 (0.05)	15.98 (0.05)	5	MKO
SDS 1254−0122..............	12 54 53.9	−01 22 47	T2.0	25	0.08490 (0.00190)	8	14.66 (0.03)	14.13 (0.03)	13.84 (0.03)	5	MKO
SDS 1021−0304[b]............	10 21 09.7	−03 04 20	T3.0	25	0.03440 (0.00460)	7	15.88 (0.03)	15.41 (0.03)	15.26 (0.05)	5	MKO
SDS 1750+1759..............	17 50 33.0	+17 59 04	T3.5	25	0.03624 (0.00453)	9	16.14 (0.05)	15.94 (0.05)	16.02 (0.05)	3	MKO
2MA 2254+3123	22 54 18.8	+31 23 49	T4.0	25	. . .	. . .	15.26 (0.05)	15.02 (0.08)	14.90 (0.15)	1	2MA
SDS 0207+0000................	02 07 42.8	+00 00 56	T4.5	25	0.03485 (0.00987)	9	16.63 (0.05)	16.66 (0.05)	16.62 (0.05)	3	MKO

TABLE 1—*Continued*

Name	R.A. (J2000.0)	Decl. (J2000.0)	Spectral Type[a]	Spectral Type Ref.	π (error) (arcsec)	π Ref.	J (error)	H (error)	K_s (error)	JHK Ref.	Photometric System
2MA 0559−1404............	05 59 19.1	−14 04 48	T4.5	25	0.09770 (0.00130)	8	13.57 (0.03)	13.64 (0.03)	13.73 (0.03)	3	MKO
SDS 0926+5847[b]	09 26 15.4	+58 47 21	T4.5	25	. . .	. . .	15.47 (0.03)	15.42 (0.03)	15.50 (0.03)	3	MKO
2MA 0755+2212	07 55 48.0	+22 12 18	T5.0	25	. . .	. . .	15.46 (0.03)	15.70 (0.03)	15.86 (0.03)	4	MKO
2MA 2339+1352	23 39 10.1	+13 52 30	T5.0	25	. . .	. . .	15.81 (0.03)	16.00 (0.03)	16.17 (0.03)	4	MKO
2MA 2356−1553............	23 56 54.7	−15 53 10	T5.0	25	0.06897 (0.00342)	9	15.48 (0.03)	15.70 (0.03)	15.73 (0.03)	4	MKO
2MA 1534−2952[b]	15 34 49.8	−29 52 27	T5.5	25	0.07360 (0.00120)	7	14.60 (0.03)	14.74 (0.03)	14.91 (0.03)	4	MKO
2MA 1546−3325............	15 46 27.1	−33 25 11	T5.5	25	0.08800 (0.00190)	7	15.63 (0.05)	15.45 (0.09)	15.49 (0.18)	1	2MA
SDS 1110+0116............	11 10 10.0	+01 16 13	T5.5	25	. . .	. . .	16.12 (0.05)	16.22 (0.05)	16.05 (0.05)	3	MKO
2MA 0243−2453............	02 43 13.7	−24 53 29	T6.0	25	0.09362 (0.00363)	9	15.13 (0.03)	15.39 (0.03)	15.34 (0.03)	4	MKO
2MA 1225−2739[b]	12 25 54.3	−27 39 47	T6.0	25	0.07510 (0.00250)	7	14.88 (0.03)	15.17 (0.03)	15.28 (0.03)	3	MKO
SDS 1624+0029............	16 24 14.4	+00 29 16	T6.0	25	0.09090 (0.00120)	7	15.66 (0.05)	15.83 (0.05)	15.90 (0.11)	6	2MA
2MA 0937+2931	09 37 34.7	+29 31 42	T6p	25	0.16284 (0.00388)	9	14.58 (0.04)	14.67 (0.03)	15.39 (0.06)	4	MKO
2MA 1047+2124	10 47 53.9	+21 24 23	T6.5	25	0.09473 (0.00381)	9	15.77 (0.04)	15.83 (0.03)	16.20 (0.03)	3	MKO
2MA 1237+6526	12 37 39.2	+65 26 15	T6.5	25	0.09607 (0.00478)	9	16.17 (0.05)	16.21 (0.05)	16.72 (0.06)	6	2MA
SDS 1346−0031..............	13 46 46.5	−00 31 50	T6.5	25	0.06830 (0.00230)	7	15.49 (0.05)	15.84 (0.05)	15.73 (0.05)	3	MKO
2MA 0727+1710	07 27 18.2	+17 10 01	T7.0	25	0.11014 (0.00234)	9	15.19 (0.03)	15.67 (0.03)	15.69 (0.03)	4	MKO
2MA 1553+1532[b]	15 53 02.2	+15 32 36	T7.0	25	. . .	. . .	15.34 (0.03)	15.76 (0.03)	15.95 (0.03)	4	MKO
2MA 1217−0311............	12 17 11.1	−03 11 13	T7.5	25	0.09080 (0.00220)	7	15.56 (0.03)	15.98 (0.03)	15.92 (0.03)	3	MKO
GJ 570D..........................	14 57 15.0	−21 21 48	T7.5	25	0.16930 (0.00170)	10	15.32 (0.05)	15.27 (0.09)	15.24 (0.16)	1	2MA
2MA 0415−0935.............	04 15 19.5	−09 35 06	T8.0	25	0.17434 (0.00276)	9	15.32 (0.03)	15.70 (0.04)	15.83 (0.03)	4	MKO
ϵ Ind BC[b]	22 04 10.5	−56 46 58	T1.0+T6.0	25	0.27580 (0.00069)	10	11.91 (0.02)	11.31 (0.02)	11.21 (0.02)	1	2MA

NOTE.—Units of right ascension are hours, minutes, and seconds, and units of declination are degrees, arcminutes, and arcseconds.

[a] Unless otherwise noted, optical spectral types are used for M and L dwarfs, and infrared spectral types are used for the T dwarfs.

[b] Known binary.

REFERENCES.—*Spectral type references*: (1) Golimowski et al. 2004a, 2004b; (2) Henry et al. 1994; (3) Bessell 1991; (4) Kirkpatrick et al. 1991; (5) Henry et al. 2004; (6) Kirkpatrick et al. 1995; (7) Scholz et al. 2000; (8) Reid et al. 2003; (9) Kirkpatrick et al. 1997; (10) Basri et al. 2000; (11) Cruz et al. 2003; (12) Wilson et al. 2003; (13) Reid et al. 2000; (14) Gizis et al. 2000; (15) Kirkpatrick et al. 1999; (16) Gizis 2002; (17) Hawley et al. 2002; (18) J. D. Kirkpatrick et al. 2006, in preparation; (19) Kirkpatrick et al. 2000; (20) Kirkpatrick et al. 2001; (21) Fan et al. 2000; (22) Burgasser et al. 2003b; (23) Wilson et al. 2001; (24) Geballe et al. 2002; (25) Burgasser et al. 2005b. *Parallax references*: (1) VizieR Online Data Catalog, 1174 (W. F. van Altena, J. T. Lee, & D. Hoffleit, 1995); (2) Gould & Chaname 2004; (3) Henry et al. 2004; (4) Costa et al. 2005; (5) Reid & Gizis 2005; (6) Reid et al. 2003; (7) Tinney et al. 2003; (8) Dahn et al. 2002; (9) Vrba et al. 2004; (10) Perryman et al. 1997. *Photometry references*: (1) 2MASS; (2) Leggett 1992; (3) Leggett et al. 2002; (4) Knapp et al. 2004; (5) Leggett et al. 2000; (6) This paper.

2MA 0451−3402.—Observed to have periodic photometric variability with a period of ∼6.9 hr (Koen 2004).

2MA 0746+2000AB.—Reported to be photometrically variable with a period of 31 hr according to Gelino (2002). Its measured $v \sin i$ (Bailer-Jones 2004) is inconsistent with that rotation period, however.

2MA 2224−0158.—Noted as having an anomalously red spectrum, possibly indicative of an unusually thick condensate cloud or of low surface gravity (Cushing et al. 2005).

3. OBSERVATIONS

IRAC is a four-channel camera that obtains simultaneous broadband images at 3.6, 4.5, 5.8, and 8.0 μm (sometimes referred to as *channels* 1–4, respectively). Two nearly adjacent 5.2×5.2 fields of view in the focal plane (for 256×256 pixel detector arrays) are viewed by the four channels in pairs (3.6 and 5.8 μm; 4.5 and 8 μm). Additional details on the design and performance of IRAC can be found in Fazio et al. (2004).

Profiles of the IRAC filters are shown in Figure 1. For comparison, the profiles of the MKO L' and M' filters, as well as a model spectrum of a mid-T dwarf, are also shown to illustrate the relative band centers and bandwidths of filters in recent use to characterize the infrared colors of M, L, and T dwarfs (e.g., Leggett et al. 2002; Golimowski et al. 2004a; Knapp et al. 2004). While the IRAC 3.6 μm channel does share some similarities with the standard L filter, it is important to note that the 3.6 and 4.5 μm IRAC channels are significantly bluer than the L', M, and M' filters and/or are much broader than all of these filters. The photometry presented in this paper has been calibrated using a zero

magnitude defined by Vega in all IRAC channels (e.g., Cohen 2003; Cohen et al. 2003; Reach et al. 2005). As illustrated in Figure 1, the spectra of low and substellar mass objects have a great deal of structure within the filter bandpasses. Therefore, particularly for T dwarfs, IR fluxes measured using broadband filters are critically dependent on both the central wavelength and the
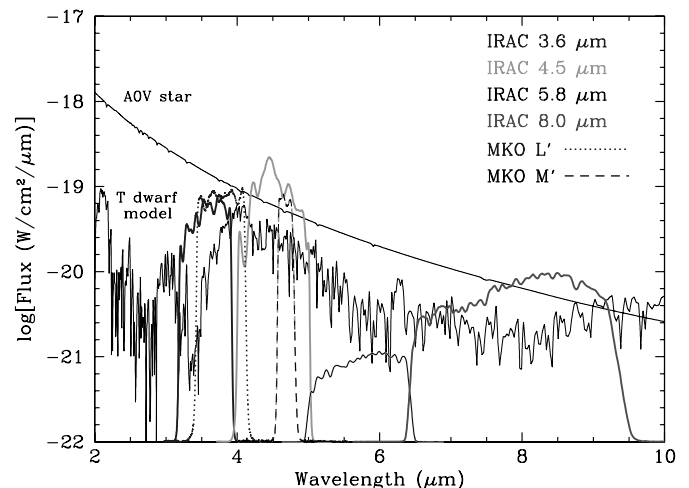

FIG. 1.—Comparison of the IRAC bandpasses with the MKO L' and M' filters in recent use for ground-based studies of M, L, and T dwarfs. Also shown for comparison is a model spectrum for a $T_{\rm eff}$ = 950 K, $g = 10^5$ cm s^{-2} ∼mid-T dwarf (Burrows et al. 2002) and that for an A0 V star. The IRAC bandpasses have been scaled to show their relative sensitivity. [*See the electronic edition of the Journal for a color version of this figure.*]

filter transmission profile. Significant color terms can be present when transforming fluxes measured in apparently similar filters from two different systems (e.g., from L' to IRAC 3.6 μm).

3.1. *Observing Strategy*

All observations in this GTO program share a common *Spitzer* Astronomical Observation Request (AOR) design. Each target was observed using the same camera modes and frame times, as well as dithering the targets over the same pixels (approximately) on the arrays. The primary motivation of this strategy was to minimize the introduction of additional uncertainties into the relative photometry for each object. Specifically, the AOR uses a five-position Gaussian dither pattern, starting with the target near the center of the array. Dithering mitigates the effects of cosmic rays and bad/hot pixels, while the small-scale-factor option for the pattern keeps the target near the center of the detectors in order to minimize spatially dependent uncertainties in the calibration of the instrument. The relative offsets for each dither position in the pattern were identical for all of the objects in the program and were distributed within a radius of $38''$ of the center/initial position. High dynamic range mode was used because the program objects cover a wide range of brightness, and the relative sensitivities of the four IRAC detectors preclude a single exposure time that will produce a good S/N and unsaturated photometry in all four channels (see also the discussion in § 3.3). The frame times of 30 and 2 s yield effective exposure times for each dither position of 26.8 and 1.2 s, respectively.

The individual observations themselves were scheduled by the *Spitzer* Science Center (SSC) and were executed over the period 2003 December 6 to 2004 November 1. The data for each target, as received from the spacecraft, were processed by the IRAC pipeline software at the SSC. This pipeline removes the electronic bias, subtracts a dark-sky image generated from observations of relatively empty sky near the ecliptic pole, flat fields the data using calibration observations of relatively blank fields near the ecliptic plane, and then linearizes the data using laboratory measurements of each pixel's response to a calibration lamp in frames of varying length.[7] The absolute calibration of IRAC is derived from aperture photometry of standard stars. This calibration is applied to the data such that the final pipeline product for each frame is in units of surface flux per steradian (i.e., Reach et al. 2005). The pipeline processing produces calibrated data for each frame in the dither pattern for each IRAC channel. This constitutes the Basic Calibrated Data (BCD) that were used for our analysis.

3.2. *Photometry*

Photometry was extracted for each source using the aperture photometry package in IRAF. To ensure the highest S/N and to minimize contamination by cosmic rays, the individual images in the dither pattern in each channel were combined using a local postpipeline software suite developed by one of us (B. M. P.). This software was used to coregister the frames in sky coordinates and then co-add the frames while rejecting temporally transient events (e.g., cosmic rays) as well as fixed-pattern noise and bad pixels. We note that caution must be used with any kind of filtering scheme to remove transients when co-adding or mosaicking IRAC data. Because the point-spread function (PSF) is under/critically sampled by the IRAC arrays, this can lead to a pixel response function (PRF) that is sharply peaked if the PSF is centered on a pixel or to a PRF with a broader, lower intensity peak if the PSF is centered at

---

[7] Additional details can be found in the IRAC Data Handbook at http://ssc.spitzer.caltech.edu/irac/data.html.

the corners of four adjacent pixels (the two extreme cases). Thus, the pixel phase (i.e., the position within a pixel) of the PSF centroid becomes important when using transient rejection based on, say, median filtering and/or sigma clipping. The large changes in the peak of the PRF for a dithered source could lead to real flux being rejected and, thus, to an artificial reduction in the count rate of the source when combining the individual frames of the dither sequence (see additional discussion in Schuster et al. 2006).

To measure the photometry, we first removed the surface flux calibration from the images by dividing by the flux conversion factor (MJy sr^{-1} per DN s^{-1}) found in the image headers of the BCD and by multiplying by the effective integration time: 26.8 or 1.2 s for the individual frames in the dither pattern and 134 or 6 s for the co-added, cleaned data. The IRAC absolute calibration is based on observations of standard stars measured with aperture photometry using a source aperture with a radius of 10 native IRAC pixels in each channel. The background was estimated using an annulus centered on the source position with an inner radius of 10 pixels and width of 10 pixels (Reach et al. 2005). Because many of the targets in our program are located in semicrowded fields, we chose to use a smaller source aperture with a radius of 4 native IRAC pixels in order to avoid contaminating flux from other, nearby sources. An additional benefit of using a smaller source aperture is an improved S/N for many of the fainter sources. For the background estimation, we used the same annulus as that defined for the IRAC absolute calibration. Photometry was extracted from both the co-added frames and the individual BCDs for each channel.

The background-subtracted net source counts were then transformed into physical units by multiplying by the flux conversion factor and then by the solid angle for each pixel, to yield fluxes for each source. This flux density is then referenced against that of Vega in each IRAC channel to put our photometry on a Vega-relative system. Because we used a source aperture of 4 native IRAC pixels in radius, an aperture correction must be applied to the photometry. Because the correction for a 4 pixel radius source aperture is not given in the IRAC Data Handbook, the aperture correction for the photometry was empirically determined by comparing our source aperture to the standard 10 pixel radius aperture using 15 relatively bright, unsaturated targets from our program. Thus, the final calibration of our data used is that of Reach et al. (2005), combined with our own aperture correction. All of the relevant numbers used to calibrate our photometry are summarized in Table 2. Table 3 summarizes the IRAC photometry for all of our targets.

3.3. *Error Analysis*

The photometry for each of our targets was measured using the coregistered, co-added, and cosmic-ray-cleaned mosaic images, and the individual BCDs in the dither pattern. We used the latter data to examine the repeatability of the photometry with a single AOR in order to gain some insight into errors associated with photometry of the co-added data. Figure 2 shows the standard deviation of the photometry from the individual BCDs for each target for each IRAC channel. All of our targets were observed using HDR mode, meaning that both a short and long frame-time exposure was taken at each position in the dither pattern. In general, we favored the use of the long-exposure (30 s frame time) BCDs over the short-exposure (2 s frame time) BCDs in our HDR AORs, unless the target object was saturated in the long-exposure frames. In a few cases where there was good S/N in both the long- and short-exposure frames, we found good agreement (within a few percent) in the calibrated photometry from both frame times. We find that the mean fluxes from the individual

TABLE 2
IRAC Photometry Calibration

	IRAC Channel			
Item	1 (3.6 μm)	2 (4.5 μm)	3 (5.8 μm)	4 (8.0 μm)
Nominal λ (μm)	3.550	4.493	5.731	7.872
BCD calibration ([MJy sr^{-1}]/[DN s^{-1}])	0.1088	0.1388	0.5952	0.2021
Point-source calibration (μJy/[DN s^{-1}])	3.813	4.800	20.891	7.070
Aperture correction (error) for 4 pixel radius (mag)	-0.084 (0.009)	-0.089 (0.006)	-0.072 (0.015)	-0.077 (0.034)
F_ν(Vega) (Jy)	280.9	179.7	115.0	64.13

measures compare very well to those measured in the mosaic images. In fact, we used this comparison as one of our checks of photometric consistency in detecting outliers in photometry of our target in the individual frames, induced by bad pixels or cosmic-ray hits.

Overall, we find that the dispersions of the individual measures used to create the mosaics are larger than those estimated using photon statistics and basic detector characteristics (e.g., read noise, gain, etc.) alone. For IRAC channels 1 and 2 these are 5 and 3 times larger, respectively, while for channels 3 and 4 they are essentially comparable, with the individual measure dispersions being only ~20% larger on average in each channel than the basic photon statistics. This is probably due in part to some camera properties that have not been fully characterized in the current calibration. These include intrapixel phase-sensitivity variations, variations in the pixel solid angle due to geometric distortions introduced by the telescope and camera optics, and variations of the spectral response over the arrays due to the tilt of the filters with respect to the optical path and the relatively wide field of view of the camera. For the latter two issues, the corrections are defined to be unity at the center of the arrays (Reach et al. 2005). Thus, while all of these effects will act to increase the dispersion of the individual measurements in our dithered data, because our observing strategy for this program keeps the target object within ~38″ of the center of the arrays, these additional uncertainties should be minimized.

We have chosen to use the standard deviation of the individual BCD measures for each source in each channel as the uncertainty of the photometry. These are the uncertainties quoted in Table 3. The number of BCDs used to construct the co-added frame for each channel and to calculate the standard deviation are also listed for each source and channel in Table 3. In terms of absolute calibration to the Vega-relative magnitude system, the uncertainty of the IRAC photometry, convolved with the additional uncertainty introduced by our aperture correction, is about 3% in IRAC channels 1–3, and 5% in channel 4 (Reach et al. 2005).

4. IRAC MAGNITUDES AND COLORS FOR LATE M, L, AND T DWARFS

Molecular features found in the infrared for low-mass stars and substellar mass objects have strengths that are a strong function of temperature and pressure. With the appropriate choice of photometric bandpasses, one can study trending as a function of color, magnitude, and spectral type as a part of characterizing the atmospheres of these objects. For example, in the near-IR, the spectra of L dwarfs are characterized by absorption from CO and H_2O, while the T dwarfs are dominated by broad absorption bands of CH_4 and H_2O, as well as collisionally induced absorption (CIA) by H_2. Thus, in near-IR photometry, M and L dwarfs become redder with decreasing T_{eff} in $J - H$ and $H - K$. The L–T dwarf transition occurs as the silicate and iron condensates (clouds)

become buried at increasing depth in the late L dwarfs. H_2O absorption begins to dominate the near-IR spectrum, leading to a bluing of the near-IR colors through the early T types. The colors then become even bluer from early T to late T with the onset and growth of CH_4 absorption and CIA H_2 in K. The overall result is that the $J - H$ and $H - K$ colors for T dwarfs become bluer with increasing spectral subtype, becoming degenerate with the colors of higher mass K and M dwarfs.

The IRAC filters were selected primarily to provide contiguous bandpasses from ~3 to 10 μm for the determination of photometric redshifts for extragalactic objects as part of the primary *Spitzer* mission objectives (Fazio et al. 2004). However, these bandpasses were also defined, in part, to provide diagnostics for the study of substellar mass objects. The bandpass for IRAC channel 1 includes much of the CH_4 fundamental absorption band (~3.3 μm). Channel 2 includes the continuum peak that is present for all stars cooler than 3000 K, making this the most sensitive IRAC channel for the study of substellar objects. Channel 2 also contains the broad but shallow CO fundamental absorption band (~4.7 μm), whose presence in the T dwarfs provides evidence for nonequilibrium chemistry models (see discussion in § 5). Channel 3 includes H_2O absorption. Finally, for channel 4, the most important molecular absorption in this bandpass is due to CH_4.

IRAC provides very precise fluxes in a wavelength regime that is poorly studied to date. For this reason, we believe it is useful to examine the IRAC data from several perspectives. First, we take a purely empirical viewpoint and limit ourselves to only the IRAC photometry to explore the IRAC colors of M, L, and T dwarfs. Next, we combine IRAC and near-IR photometry to examine the location of M, L, and T dwarfs in both color-color and color-magnitude diagrams. In § 4.3 we show the variations of near- and mid-IR colors with spectral type. Finally, in § 5, we compare color-magnitude diagrams for M, L, and T dwarfs with theoretical models.

4.1. Color-Magnitude and Color-Color Diagrams

4.1.1. IRAC Photometry

Star formation studies often use plots of $[3.6]-[4.5]$ versus $[4.5]-[5.8]$ or $[3.6]-[4.5]$ versus $[5.8]-[8.0]$ in order to identify young stars with warm circumstellar dust disks and envelopes. This technique is particularly effective because normal stars have essentially Rayleigh-Jeans spectra at IRAC wavelengths and hence have colors very near zero. Stars with warm dust disks have significantly red colors in IRAC wavelengths, and thus separate from older, dust-free stars. Late M, L, and T dwarfs, however, depart from this convenient scenario because they are cool enough to have photospheres sufficiently polluted by molecules that their spectra depart greatly from blackbodies.

As shown in Figure 3, L dwarfs have $[3.6]-[4.5]$ colors that remain close to zero, but have $[4.5]-[5.8]$ colors that become

TABLE 3
IRAC Photometry and Colors of Late-type M, L, and T Dwarfs

Name	Spectral Type	[3.6] (error)	n	[4.5] (error)	n	[5.8] (error)	n	[8.0] (error)	n	[3.6]−[4.5]	[4.5]−[5.8]	[5.8]−[8.0]	Notes
GJ 1001A......................	M3.5	7.45 (0.03)	5	7.40 (0.03)	5	7.37 (0.01)	5	7.36 (0.01)	5	0.05	0.04	0.01	1
GJ 1093..........................	M5.0	7.86 (0.03)	4	7.84 (0.02)	5	7.76 (0.01)	5	7.74 (0.01)	5	0.02	0.09	0.02	1
GJ 1156..........................	M5.0	7.24 (0.03)	5	7.16 (0.02)	5	7.10 (0.01)	5	7.08 (0.01)	5	0.08	0.06	0.02	1
GJ 1002..........................	M5.5	7.07 (0.01)	5	7.01 (0.01)	5	6.97 (0.02)	5	6.95 (0.01)	5	0.05	0.04	0.02	2
LHS 288..........................	M5.5	7.31 (0.03)	5	7.25 (0.04)	5	7.27 (0.01)	5	7.20 (0.01)	5	0.06	−0.03	0.07	2
GJ 412B	M5.5	7.38 (0.01)	5	7.29 (0.05)	5	7.23 (0.02)	5	7.18 (0.00)	5	0.08	0.06	0.05	2
GJ 1111	M6.5	6.84 (0.02)	5	6.84 (0.04)	5	6.76 (0.05)	5	6.74 (0.01)	5	0.00	0.08	0.02	3
LHS 292..........................	M6.5	7.52 (0.02)	5	7.51 (0.02)	5	7.46 (0.02)	5	7.42 (0.01)	5	0.01	0.05	0.03	2
SO 0253+1652................	M7.0	7.12 (0.01)	3	7.10 (0.02)	5	7.05 (0.01)	5	7.02 (0.01)	5	0.02	0.04	0.03	2
LHS 3003........................	M7.0	8.47 (0.02)	5	8.49 (0.01)	5	8.39 (0.02)	5	8.36 (0.01)	5	−0.02	0.10	0.03	4, 5
GJ 644C	M7.0	8.37 (0.02)	5	8.38 (0.02)	5	8.28 (0.02)	5	8.24 (0.02)	5	−0.01	0.11	0.03	4, 5
LHS 132..........................	M8.0:	9.64 (0.02)	5	9.62 (0.02)	5	9.52 (0.02)	5	9.48 (0.01)	4	0.02	0.10	0.04	4, 5
LHS 2021........................	M8.0	10.32 (0.02)	5	10.35 (0.01)	5	10.24 (0.01)	5	10.20 (0.01)	5	−0.04	0.11	0.03	4
GJ 752B	M8.0	8.29 (0.02)	5	8.30 (0.03)	5	8.15 (0.01)	5	8.14 (0.00)	5	−0.01	0.15	0.02	4, 5
2MA 1835+3259	M8.5	8.55 (0.02)	5	8.55 (0.01)	5	8.39 (0.01)	5	8.29 (0.01)	5	0.00	0.16	0.10	4, 5
LP 944−020	M9.0	8.87 (0.03)	5	8.79 (0.01)	5	8.59 (0.01)	5	8.42 (0.01)	5	0.08	0.19	0.18	4, 5, 6
LHS 2065........................	M9.0	9.41 (0.02)	5	9.39 (0.03)	5	9.22 (0.01)	5	9.13 (0.01)	5	0.02	0.17	0.09	4, 5
LHS 2924........................	M9.0	10.16 (0.02)	5	10.16 (0.01)	5	9.97 (0.01)	5	9.81 (0.01)	5	0.00	0.19	0.16	4
DEN 0021−4244	M9.5	11.62 (0.01)	5	11.59 (0.01)	5	11.43 (0.04)	5	11.30 (0.04)	5	0.03	0.16	0.14	. . .
BRI 0021−0214	M9.5	9.94 (0.03)	4	9.91 (0.03)	4	9.72 (0.01)	5	9.55 (0.01)	4	0.02	0.20	0.17	4, 5
2MA 1204+3212	L0.0	11.93 (0.01)	5	11.95 (0.01)	5	11.82 (0.01)	5	11.65 (0.03)	5	−0.01	0.13	0.17	. . .
2MA 0320−0446.............	L0.5(IR)	11.50 (0.03)	5	11.44 (0.01)	5	11.29 (0.02)	5	11.18 (0.01)	4	0.06	0.15	0.11	. . .
2MA 0451−3402.............	L0.5	11.66 (0.04)	5	11.66 (0.03)	5	11.52 (0.02)	5	11.30 (0.04)	5	−0.01	0.14	0.22	7
2MA 0746+2000AB[a].....	L0.5	9.86 (0.02)	5	9.90 (0.04)	4	9.72 (0.01)	4	9.57 (0.01)	5	−0.03	0.18	0.15	4, 5
2MA 1300+1912	L1.0	10.96 (0.02)	5	11.00 (0.03)	5	10.86 (0.01)	5	10.73 (0.03)	5	−0.04	0.14	0.14	. . .
2MA 1439+1929	L1.0	10.91 (0.02)	5	10.93 (0.03)	5	10.82 (0.03)	5	10.67 (0.02)	5	−0.02	0.11	0.15	4, 5
2MA 1555−0956.............	L1.0	10.83 (0.01)	5	10.88 (0.01)	5	10.76 (0.02)	5	10.63 (0.01)	5	−0.05	0.12	0.12	. . .
2MA 1645−1319.............	L1.5	10.48 (0.04)	5	10.52 (0.02)	5	10.36 (0.01)	5	10.20 (0.01)	5	−0.04	0.16	0.15	4
2MA 1017+1308	L2.0:	12.03 (0.01)	5	12.05 (0.03)	5	11.85 (0.04)	4	11.70 (0.03)	5	−0.02	0.20	0.16	. . .
2MA 1155−3727.............	L2.0	10.74 (0.02)	5	10.75 (0.02)	5	10.58 (0.01)	5	10.42 (0.02)	5	−0.01	0.17	0.16	4
Kelu-1[a]	L2.0	10.92 (0.05)	5	10.90 (0.04)	5	10.73 (0.01)	5	10.61 (0.02)	5	0.02	0.17	0.12	4, 5
DEN 1058−1548.............	L3.0	11.76 (0.02)	5	11.77 (0.02)	5	11.60 (0.02)	5	11.50 (0.02)	5	−0.01	0.17	0.10	. . .
2MA 1506+1321	L3.0	10.86 (0.02)	5	10.85 (0.06)	5	10.69 (0.04)	5	10.58 (0.01)	5	0.01	0.17	0.10	4, 5
2MA 1721+3344	L3.0	11.58 (0.02)	5	11.62 (0.02)	5	11.49 (0.04)	5	11.40 (0.02)	5	−0.04	0.13	0.10	8
SDS 2028+0052.............	L3.0	11.97 (0.02)	5	12.03 (0.02)	5	11.83 (0.03)	5	11.71 (0.03)	5	−0.06	0.20	0.13	. . .
2MA 2104−1037.............	L3.0	11.55 (0.03)	5	11.62 (0.01)	5	11.44 (0.03)	5	11.29 (0.04)	4	−0.07	0.18	0.15	. . .
2MA 0036+1821	L3.5	10.19 (0.03)	5	10.24 (0.01)	5	10.10 (0.02)	5	10.06 (0.01)	5	−0.05	0.15	0.04	4
DEN 1539−0520.............	L4.0:	11.65 (0.02)	5	11.75 (0.04)	5	11.61 (0.05)	5	11.60 (0.05)	5	−0.10	0.14	0.01	. . .
2MA 0141+1804	L4.5(IR)	11.89 (0.04)	4	11.92 (0.01)	5	11.76 (0.04)	5	11.67 (0.03)	5	−0.03	0.15	0.09	9
2MA 0652+4710	L4.5	10.50 (0.01)	5	10.50 (0.01)	5	10.23 (0.01)	5	10.12 (0.02)	5	0.00	0.27	0.11	4
2MA 2224−0158.............	L4.5	11.05 (0.02)	5	11.14 (0.02)	5	10.85 (0.01)	5	10.81 (0.02)	5	−0.09	0.30	0.03	. . .
GJ 1001BC[a].....................	L5.0	10.36 (0.01)	5	10.47 (0.01)	5	10.14 (0.03)	5	10.13 (0.02)	5	−0.11	0.33	0.01	10
SDS 0539−0059.............	L5.0	11.49 (0.02)	5	11.60 (0.02)	5	11.35 (0.03)	4	11.20 (0.04)	4	−0.11	0.25	0.14	11
2MA 0835−0819.............	L5.0	10.06 (0.03)	5	10.06 (0.02)	5	9.79 (0.01)	5	9.73 (0.00)	5	0.00	0.28	0.05	4
2MA 0908+5032	L5.0	11.67 (0.02)	5	11.66 (0.01)	5	11.39 (0.01)	4	11.13 (0.03)	5	0.01	0.27	0.26	. . .
2MA 1507−1627.............	L5.0	10.27 (0.03)	5	10.40 (0.02)	5	10.14 (0.02)	5	9.99 (0.01)	5	−0.14	0.26	0.15	4, 5
SDS 1331−0116.............	L6.0	12.96 (0.02)	4	13.13 (0.02)	5	12.95 (0.08)	4	12.62 (0.06)	4	−0.17	0.18	0.33	. . .
2MA 1515+4847	L6.0(IR)	11.31 (0.02)	5	11.33 (0.02)	5	11.07 (0.02)	5	10.83 (0.02)	5	−0.02	0.26	0.24	. . .
2MA 0717+5705	L6.5(IR)	11.95 (0.01)	4	11.96 (0.01)	5	11.76 (0.01)	5	11.68 (0.01)	4	−0.01	0.19	0.08	. . .
2MA 1526+2043	L7.0	12.79 (0.02)	5	12.87 (0.03)	5	12.60 (0.11)	5	12.32 (0.04)	5	−0.07	0.26	0.29	. . .
2MA 1728+3948[a]..........	L7.0	12.72 (0.02)	5	12.66 (0.01)	5	12.29 (0.04)	4	12.13 (0.03)	5	0.06	0.37	0.15	. . .
2MA 0825+2115	L7.5	11.70 (0.02)	5	11.59 (0.01)	5	11.16 (0.01)	4	10.93 (0.02)	5	0.11	0.43	0.23	. . .
DEN 0255−4700.............	L8.0	10.29 (0.02)	5	10.20 (0.02)	5	9.89 (0.01)	5	9.61 (0.01)	5	0.09	0.32	0.28	4, 5
SDS 0857+5708.............	L8.0	11.62 (0.00)	4	11.44 (0.02)	5	11.02 (0.01)	5	10.74 (0.02)	5	0.19	0.42	0.28	. . .
GJ 337CD[a]......................	L8.0	12.50 (0.02)	4	12.33 (0.02)	4	11.96 (0.08)	4	11.95 (0.05)	4	0.18	0.36	0.02	. . .
2MA 1632+1904	L8.0	12.70 (0.03)	5	12.65 (0.02)	5	12.24 (0.04)	5	12.00 (0.04)	4	0.05	0.41	0.24	. . .
2MA 0532+8246	sdL	13.37 (0.03)	5	13.22 (0.02)	5	13.23 (0.10)	4	13.03 (0.10)	4	0.15	−0.02	0.20	. . .
SDS 0423−0414[a]	T0.0	11.73 (0.02)	4	11.58 (0.02)	5	11.30 (0.01)	5	11.01 (0.03)	5	0.14	0.29	0.28	. . .
SDS 0151+1244.............	T0.5	14.06 (0.02)	5	13.91 (0.02)	5	13.62 (0.11)	5	13.34 (0.18)	4	0.16	0.29	0.28	. . .
SDS 0837−0000.............	T1.0	14.76 (0.03)	5	14.60 (0.01)	5	14.41 (0.13)	5	14.22 (0.14)	3	0.16	0.18	0.20	. . .
SDS 1254−0122.............	T2.0	12.63 (0.01)	5	12.39 (0.01)	4	11.99 (0.05)	5	11.75 (0.04)	5	0.24	0.40	0.24	. . .
SDS 1021−0304[a]	T3.0	14.16 (0.02)	5	13.80 (0.02)	5	13.58 (0.12)	5	13.16 (0.11)	5	0.36	0.22	0.42	. . .
SDS 1750+1759..............	T3.5	14.95 (0.03)	5	14.46 (0.02)	5	14.15 (0.23)	5	13.93 (0.23)	5	0.50	0.30	0.22	. . .
2MA 2254+3123	T4.0	13.92 (0.03)	5	13.28 (0.01)	5	13.05 (0.10)	5	12.78 (0.10)	5	0.64	0.23	0.27	. . .
SDS 0207+0000..............	T4.5	15.59 (0.06)	5	14.98 (0.05)	5	14.67 (0.20)	4	14.17 (0.19)	4	0.60	0.32	0.49	. . .
2MA 0559−1404.............	T4.5	12.67 (0.03)	5	11.93 (0.02)	5	11.73 (0.02)	5	11.42 (0.02)	5	0.75	0.20	0.31	. . .

TABLE 3—*Continued*

Name	Spectral Type	[3.6] (error)	n	[4.5] (error)	n	[5.8] (error)	n	[8.0] (error)	n	[3.6]−[4.5]	[4.5]−[5.8]	[5.8]−[8.0]	Notes
SDS 0926+5847[a]	T4.5	14.48 (0.03)	5	13.71 (0.02)	5	13.55 (0.11)	5	13.32 (0.06)	4	0.77	0.16	0.23	...
2MA 0755+2212	T5.0	14.54 (0.03)	5	13.45 (0.03)	5	13.48 (0.10)	5	12.93 (0.22)	4	1.08	−0.03	0.55	...
2MA 2339+1352	T5.0	14.82 (0.04)	5	13.95 (0.04)	5	13.98 (0.03)	4	13.80 (0.20)	4	0.87	−0.04	0.18	...
2MA 2356−1553	T5.0	14.69 (0.03)	5	13.69 (0.04)	5	13.57 (0.08)	5	13.21 (0.17)	5	1.00	0.12	0.36	...
2MA 1534−2952[a]	T5.5	13.63 (0.04)	5	12.71 (0.02)	5	12.73 (0.05)	5	12.36 (0.08)	5	0.92	−0.02	0.37	8
2MA 1546−3325	T5.5	14.22 (0.05)	5	13.39 (0.03)	5	13.44 (0.15)	4	13.38 (0.10)	4	0.83	−0.05	0.07	...
SDS 1110+0116	T5.5	14.71 (0.03)	4	13.88 (0.02)	4	13.43 (0.07)	5	13.21 (0.16)	5	0.83	0.45	0.22	...
2MA 0243−2453............	T6.0	13.90 (0.01)	5	12.95 (0.03)	5	12.71 (0.05)	4	12.27 (0.05)	4	0.95	0.24	0.44	...
2MA 1225−2739[a]	T6.0	13.84 (0.02)	5	12.75 (0.01)	5	12.84 (0.10)	5	12.24 (0.02)	5	1.09	−0.09	0.60	...
SDS 1624+0029..............	T6.0	14.30 (0.03)	5	13.08 (0.02)	5	13.25 (0.08)	5	12.84 (0.09)	5	1.22	−0.17	0.41	...
2MA 0937+2931	T6p	13.10 (0.03)	5	11.64 (0.04)	5	12.32 (0.02)	4	11.73 (0.04)	5	1.47	−0.68	0.58	...
2MA 1047+2124	T6.5	14.39 (0.06)	5	12.95 (0.04)	5	13.52 (0.07)	5	12.91 (0.10)	5	1.44	−0.57	0.61	...
2MA 1237+6526	T6.5	14.39 (0.03)	4	12.93 (0.03)	5	13.42 (0.06)	5	12.78 (0.11)	5	1.45	−0.49	0.65	...
SDS 1346−0031..............	T6.5	14.53 (0.04)	5	13.60 (0.02)	5	13.40 (0.11)	5	13.13 (0.17)	5	0.93	0.19	0.28	...
2MA 0727+1710	T7.0	14.41 (0.02)	5	13.01 (0.01)	5	13.24 (0.06)	5	12.64 (0.11)	5	1.40	−0.23	0.60	...
2MA 1553+1532[a]	T7.0	14.42 (0.01)	5	13.08 (0.02)	3	13.30 (0.10)	5	12.65 (0.10)	4	1.35	−0.23	0.66	...
2MA 1217−0311.............	T7.5	14.19 (0.03)	5	13.23 (0.02)	5	13.34 (0.07)	5	12.95 (0.18)	5	0.96	−0.12	0.39	...
GJ 570D........................	T7.5	13.80 (0.04)	5	12.12 (0.02)	5	12.77 (0.11)	5	11.97 (0.07)	5	1.68	−0.64	0.80	...
2MA 0415−0935............	T8.0	14.10 (0.03)	5	12.29 (0.02)	5	12.87 (0.07)	5	12.11 (0.05)	5	1.82	−0.58	0.76	...
ε Ind BC[a]	T1.0+T6.0	9.97 (0.01)	10	9.44 (0.02)	10	9.39 (0.03)	10	8.98 (0.04)	10	0.53	0.04	0.41	...

Notes.—(1) Source saturated in all four IRAC channels in 30 s FRAMETIME data; 2 s FRAMETIME data used instead; (2) GTO program PID 33 target; 2 s FRAMETIME data; (3) GTO program PID 33 target; 0.6 s FRAMETIME data; (4) Channel 1 saturated for 30 s FRAMETIME data; used 2 s FRAMETIME data for this channel; (5) Channel 2 saturated for 30 s FRAMETIME data; used 2 s FRAMETIME data for this channel; (6) GTO program PID 33 target; (7) Target source aperture possibly contaminated by flux from another nearby source; (8) Target in crowded field; some contamination of source aperture by other nearby sources possible; (9) *Spitzer* AOR target name incorrectly reads "2MA 1410+1804"; (10) Wings of GJ 1001 PSF may contaminate source aperture for target; however, 2 s FRAMETIME data for channels 1 and 2 agree well with the 30 s FRAMETIME data; (11) Strong nebulosity in background, especially in channel 4.

[a] Known binary.

significantly bluer. For the T dwarfs, the strong redward trend in [3.6]−[4.5] is the result of CH_4 absorption removing increasing amounts of flux from the 3.6 μm bandpass as T_{eff} decreases. On the other hand, [4.5]−[5.8] trends strongly blueward for the T dwarfs, reflecting the strengthening of H_2O absorption with decreasing T_{eff} in the 5.8 μm bandpass relative to the CO absorption in the 4.5 μm bandpass.

Fig. 2.—Repeatability of photometry for targets vs. their calibrated magnitudes for the four IRAC channels. Shown here are the standard deviations of the individual observations in the AOR dither pattern (five for most objects) vs. the calibrated magnitude derived from the co-addition of those individual observations. For the 5.8 and 8.0 μm channels, the 3 σ limiting magnitude for a high zodiacal background for a 30 s frame time is indicated (15.4 and 14.5, respectively; see footnote 7). For the 3.6 and 4.5 μm channels, the 3 σ limiting magnitudes would be located off the right of the plots at 18.9 and 17.9, respectively.
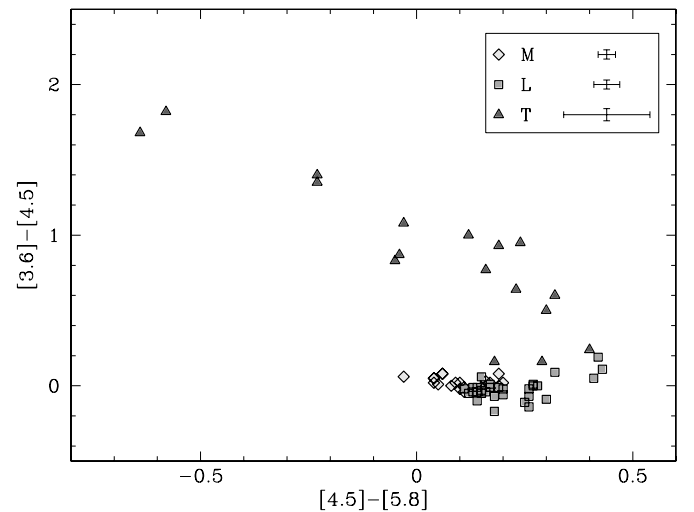

Fig. 3.—Color-color diagram of [3.6]−[4.5] vs. [4.5]−[5.8] for all of the sources in our M, L, and T dwarf sample, excluding known binaries and spectrally peculiar objects. As indicated in the legend, different plot symbols and colors are used to represent the M dwarfs (*diamonds*), L dwarfs (*squares*), and T dwarfs (*triangles*). The error bars to the right of each plot symbol in the legend represent the median values for each spectral type for the color indices used in this figure. [*See the electronic edition of the Journal for a color version of this figure.*]
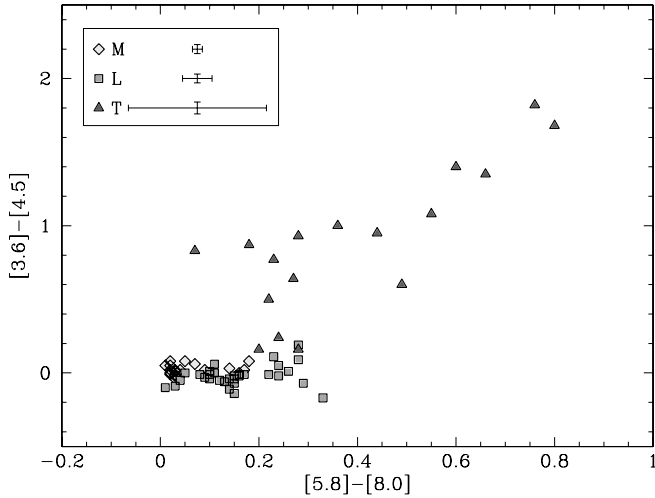
Fig. 4.—Similar to Fig. 3, except in this case we show the [3.6]−[4.5] vs. [5.8]−[8.0] color-color diagram for the same objects. [*See the electronic edition of the Journal for a color version of this figure.*]

For [3.6]−[4.5] versus [5.8]−[8.0] (Fig. 4), the M and L dwarfs show about the same range of color in [5.8]−[8.0] as in [4.5]−[5.8], but in this case there appears to be more overlap in the dispersion between these two types. Again, however, it is the T dwarfs that stand out in this plot, with both the [3.6]−[4.5] and [5.8]−[8.0] color indices trending strongly redward for decreasing T_{eff}. For the latter color index, the H_2O feature in the 5.8 μm bandpass apparently decreases the flux in this filter faster than the weaker CH_4 absorption band in the broader IRAC 8.0 μm bandpass.

To further explore the trending in the IRAC colors, we provide several variants on one specific IRAC color-color diagram: a plot of [4.5]−[5.8] versus [3.6]−[8.0]. In the first of these plots, Figure 5a shows our sample (excluding binaries and spectrally peculiar dwarfs) with symbols corresponding to the object's spectral type. Figure 5a illustrates that the three spectral types inhabit relatively distinct parts of color-color space, with the [3.6]−[8.0] color becoming progressively redder for later spectral types (i.e., that it correlates with effective temperature), whereas the [4.5]−[5.8] color is approximately constant for M and L dwarfs, but turns sharply blueward with later T types. There is not a one-to-one correspondence between spectral type and IRAC color, however: the M and L types overlap in their IRAC colors, whereas the T dwarfs appear to have a very large scatter in their colors. Are these effects simply "noise," or are they indicative of complexity in the spectra of these stars beyond that attributable to just spectral type?

To address these questions, we construct several other versions of Figure 5a but now isolating specific spectral subtype ranges. Figure 5b shows the location of "early" and late M dwarfs in this color-color plane, and illustrates that at least for our sample of stars, field M dwarfs with spectral type M8 and earlier have IRAC colors essentially consistent with zero, with only the M8.5 and later M dwarfs having significantly nonzero IRAC colors. It is only the stars in the latter subtype range that overlap in color with the L dwarfs. Figure 5c similarly isolates several L dwarf subtypes. We have combined the L0 through L3.5 dwarfs into one group because we see no significant variation in IRAC color within this subtype range; however, the IRAC colors of these early L dwarfs are significantly different from the colors of M dwarfs with type earlier than M8. The L4 and L4.5 dwarfs appear to be a transition class, with two dwarfs of this type having IRAC colors like those of earlier type L dwarfs, while the other two are signifi-

cantly redder, particularly in their [4.5]−[5.8] color. The L7.5 to L8 dwarfs have redder colors than earlier L dwarfs, and have [4.5]−[5.8] colors that are redder, on average, than even the early T dwarfs.

Figure 5d highlights the IRAC colors of T dwarfs. The early T dwarfs have [3.6]−[8.0] colors that overlap with the latest L dwarfs, but they are displaced blueward in [4.5]−[5.8] color from those dwarfs. In general, the T dwarfs show a progression, with their [3.6]−[8.0] color becoming redder and their [4.5]−[5.8] color becoming bluer with later T subtype. The T5 and T6 subtypes appear to be transitional, with a relatively large spread in [3.6]−[8.0] color for the T5 dwarfs and, in comparison, colors for the two T6 dwarfs in our sample that are closer to those of the T4 dwarfs than the T7−T8 dwarfs.

Finally, in Figure 5e, we show the relative colors of those objects in our sample that are considered spectrally peculiar or unusual. These include the lone sdL in our sample (2MA 0532+8246) and the lone T dwarf with a peculiar designation in its spectral type (T6p, 2MA 0937+2931). The other T dwarfs in the figure have been noted in the literature as being spectrally unusual. For the latter, how much of their peculiarity is due to atmospheric anomalies (i.e., metallicity) or multiplicity remains to be seen. For example, only recently has the unusual spectrum of 2MA 0423−0414 been revealed to be a composite spectrum of an ∼L6 plus ∼T2 close binary system (Burgasser et al. 2005b). Nevertheless, these objects as a whole seem to have discrepant colors when compared to other L and T dwarfs, particularly for 2MA 0532+8246 (sdL), 2MA 0937+2931 (T6p), and 2MA 1217−0311 (T7.5).

4.1.2. *IRAC Photometry Combined with JHK Photometry*

The combination of IRAC broadband photometry with near-IR photometry[8] breaks the degeneracy of the M and L dwarf colors. In a plot of K_s−[3.6] versus [3.6]−[4.5] (Fig. 6), the K_s−[3.6] color index shows a clear trend redward for the M and L dwarfs, well correlated with spectral type. For the T dwarfs, this same index trends over a more narrow range of color for increasing subtype. Although the K_s−[3.6] color index is almost degenerate, the [3.6]−[4.5] color index still spreads them nicely in Figure 6. Because pressure-induced H_2 absorption affects the K_s band in particular and is stronger if gravity is high or metallicity is low, this can introduce scatter in K_s. This is likely the major contributor to the large scatter in color seen with the same spectral subclass in the mid- and late T dwarfs (see also § 4.3 for the trending of color vs. spectral type for these two color indices). For K_s−[4.5] versus [3.6]−[4.5] (Fig. 7), the same breaking of degeneracy and range of color is seen for the M and L dwarfs in K_s−[4.5] as for K_s−[3.6]; however, in this case the T dwarfs show a strong redward trend, with a spread of ∼2.5 mag in K_s−[4.5]. The relative amount of scatter in the color index for the mid- and late T dwarfs remains the same as that seen for K_s−[3.6] in Figure 6.
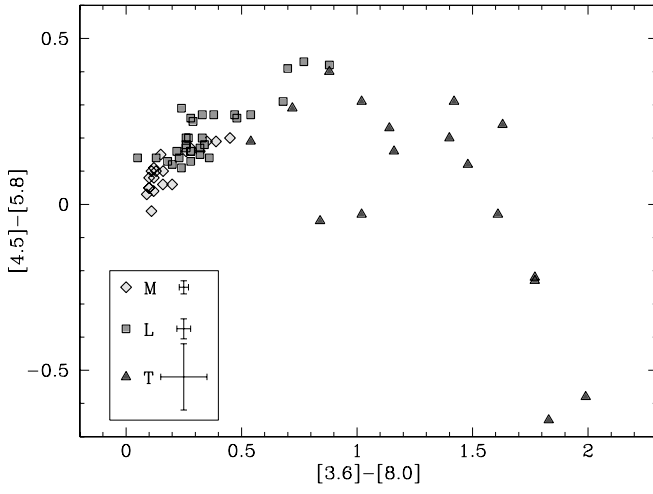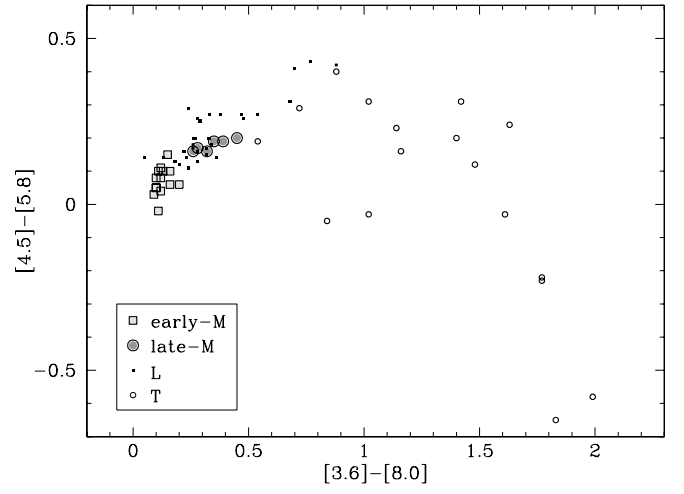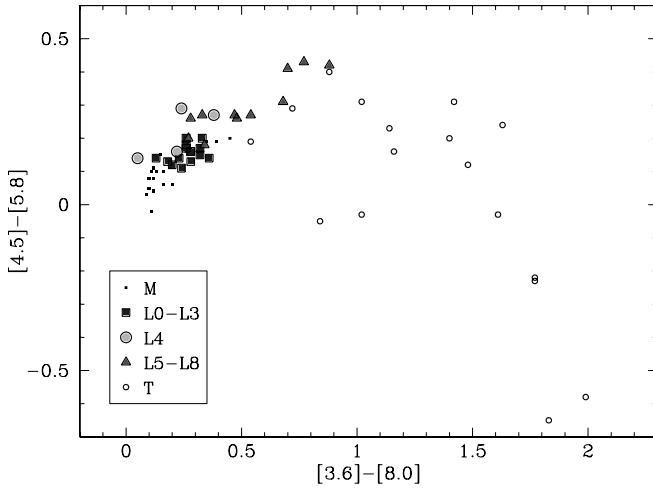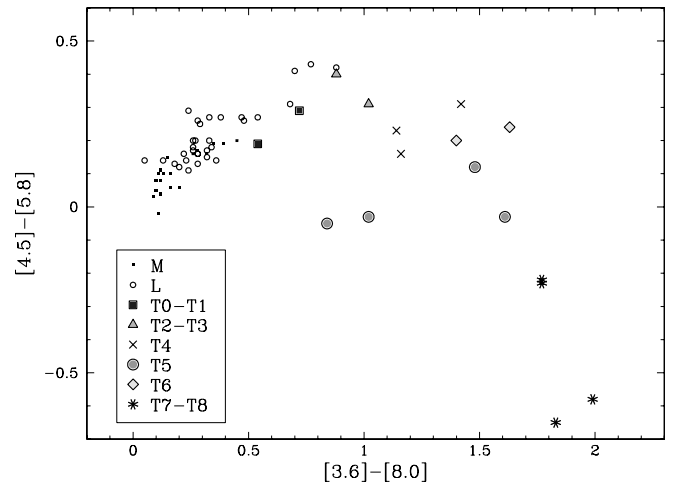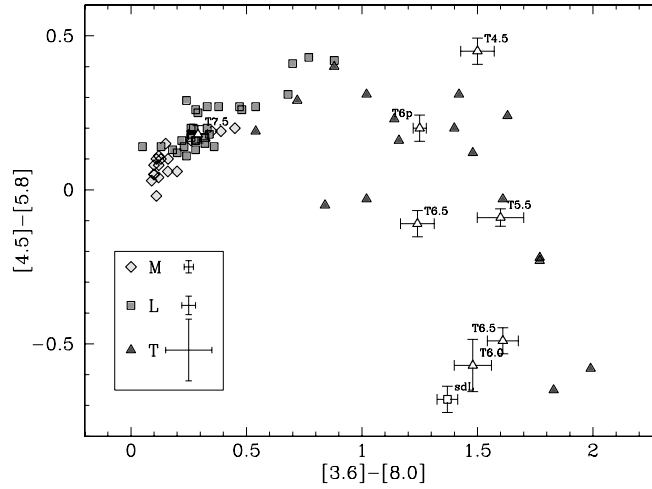
Fig. 5a

Fig. 5b

Fig. 5c

Fig. 5d

Fig. 5e

Fig. 5.—Color-color diagram of [3.6]−[8.0] vs. [4.5]−[5.8]. (*a*) Same plot symbols and objects as plotted in Fig. 3. (*b*) Same data as in (*a*), except larger symbols show the region of color-color space occupied by spectral types <M8 (*large squares*) and M8−M9 (*large circles*). (*c*) In this case, the shaded symbols show a clear separation in color-color space for early L types (L0−L3) (*large squares*) and late L (L5−L8) (*large triangles*). The L4 dwarfs (*large circles*) appear to form a transition class between the early and late types. (*d*) The breakout of the T dwarfs shows that for the early types T0−T1 (*large squares*), T2−T3 (*triangles*), and T4 (*crosses*), there is a trend toward redder [3.6]−[8.0] color with increasing spectral type, but little discernible change in the [4.5]−[5.8] color over these same types. The late T types T7−T8 (*asterisks*) are much redder in [3.6]−[8.0] and bluer in [4.5]−[5.8] than the early types. The T5 (*large circles*) and T6 (*diamonds*) subtypes appear to be transitional, with a relatively large spread in [3.6]−[8.0] color for the T5 dwarfs and redder [4.5]−[5.8] colors for the T6 dwarfs. (*e*) Spectrally peculiar objects in our sample. Each object is labeled with its spectral type and errors bars representing the uncertainty of the photometry. The shaded symbols are data for the same objects as shown in (*a*). [*See the electronic edition of the Journal for a color v*ersion of this figure.]
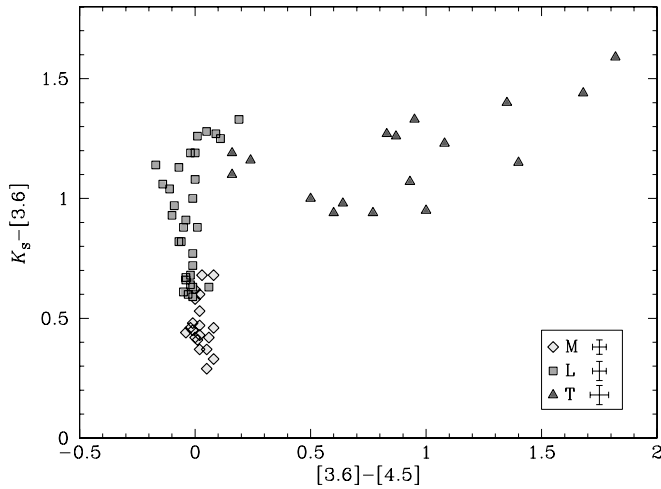
FIG. 6.—Color-color diagram of $K_s-[3.6]$ vs. $[3.6]-[4.5]$ for all of the sources in our M, L, and T dwarf sample with K-band photometry, excluding known binaries and spectrally peculiar objects. All near-IR photometry has been converted to the 2MASS JHK system using the relations of Stephens & Leggett (2004; see additional discussion in the text). The plot symbols are the same as those used in Fig. 3. [*See the electronic edition of the Journal for a color version of this figure.*]

FIG. 8.—Color-magnitude diagram of M_{K_s} vs. $K-[4.5]$ for all of the sources in our M, L, and T dwarf sample with K-band photometry and trigonometric parallaxes, excluding known binaries and spectrally peculiar objects. As in Fig. 6, all near-IR photometry has been converted to the 2MASS JHK system. Parallax references can be found in Table 1. The plot symbols are the same as those used in Fig. 3. [*See the electronic edition of the Journal for a color version of this figure.*]

4.2. *Absolute Magnitude versus Color*

For those objects in our program with trigonometric parallax measurements, we present two color-magnitude plots that could be potentially useful for identifying low-mass dwarfs in the field or as companions to other stars, using a combination of IRAC and near-IR photometry (some additional IRAC color-magnitude diagrams focusing on the T dwarfs are also presented in § 5).

In Figure 8, M_{K_s} versus $K_s-[4.5]$ shows that the colors of M, L, and T dwarfs follow a relatively smooth progression with increasing type. This is similar to the trending seen for M_{K_s} versus K_s-M' as reported by Golimowski et al. 2004a. On the other hand, in Figure 9, M_{K_s} versus $J-[4.5]$ shows an almost 2.5 mag range for the M and L dwarfs, while for the T dwarfs the $J-[4.5]$ color is essentially degenerate with the L dwarfs (and with themselves, the early T dwarfs falling in the transition area between the L dwarf and T dwarf plateaus, being degenerate not only with the mid-L dwarfs but also with mid-T types). It is only the intrin-

sic difference in luminosity that lifts the degeneracy for the $J-[4.5]$ color index.

4.3. *Color versus Spectral Type*

In the same spirit as Leggett et al. (2002), Knapp et al. (2004), and Golimowski et al. (2004a), we summarize the trending of various color indices against spectral type (Fig. 10) as a series of "postage stamp" plots. While most of this trending has already been detailed earlier in this section in the color-color and color-magnitude diagrams, plotting the indices against spectral type reveals some common themes. In particular, most of the plots in Figure 10 show breaks in the trending near the L/T boundary. The most dramatic example is in $[3.6]-[4.5]$, where the slow blueward trend through the M and early L types turns redward at mid-L (given the appearance of CH_4 absorption in the IRAC 3.6 μm

FIG. 7.—Similar to Fig. 6, except in this case we show the $K_s-[4.5]$ vs. $[3.6]-[4.5]$ color-color diagram for the same objects. [*See the electronic edition of the Journal for a color version of this figure.*]
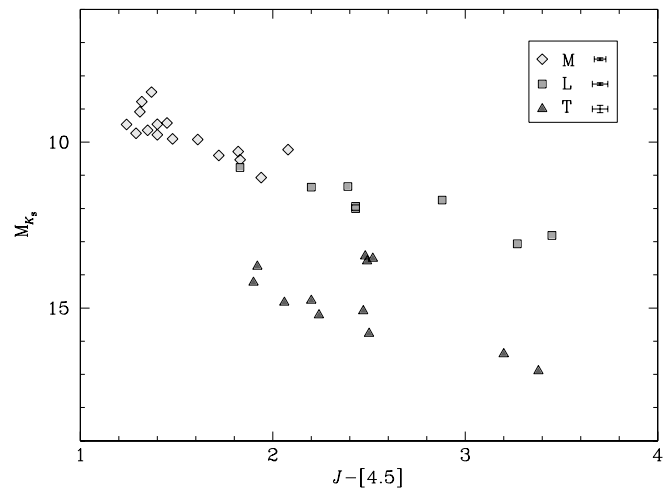

FIG. 9.—Similar to Fig. 8, except in this case we show the M_{K_s} vs. $J-[4.5]$ color-magnitude diagram for the same objects. The three T dwarfs in the region between the locus of the L dwarfs and the parallel but fainter locus of T dwarfs below have spectral types of T0.5, T1.0, and T2.0. The sequence of T dwarfs below run (*from left to right*) from T3.5 to T8. [*See the electronic edition of the Journal for a color version of this figure.*]
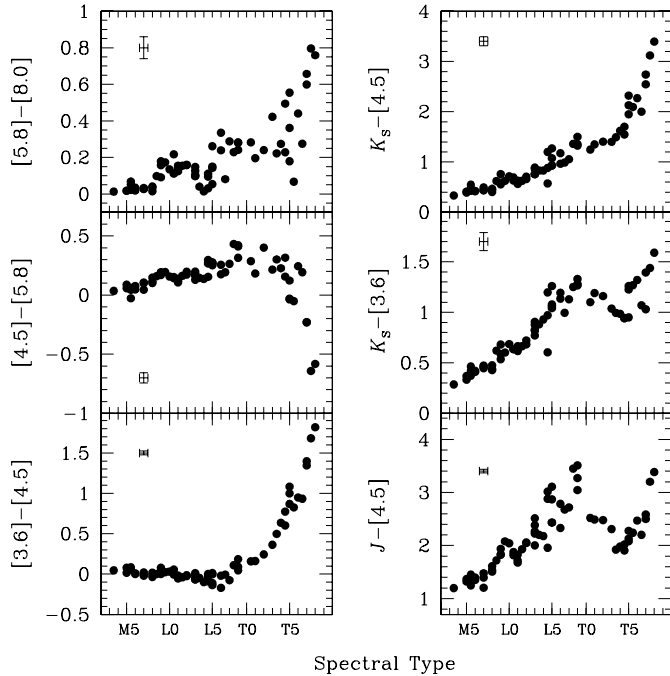
Fig. 10.—Summary of the trending seen in various color indices vs. spectral type in the same spirit as near- and mid-IR plots shown in Leggett et al. (2002), Knapp et al. (2004), and Golimowski et al. (2004a). The spectral types are the same as those used in Table 1, with optical types being used for the M and L dwarfs, and infrared types for the T dwarfs. All J- and K-band photometry is on the 2MASS system, with all transformations made using the relations of Stephen & Leggett (2004). Representative error bars for the median errors in the photometry that make up each color index and an error of ± 1 spectral subclass are shown in each plot.

bandpass) and heads strongly redward through the T types. On the other hand, the $K_s - [4.5]$ and $[4.5] - [5.8]$ plots show breaks at the mid-T types. For $[4.5] - [5.8]$, the blueward turn at mid-T presumably happens due to the strengthening of H_2O absorption with later spectral type in the IRAC 5.8 μm filter, while for $K_s - [4.5]$, the onset of both CH_4 absorption (2.2 μm overtone feature) and CIA H_2 in the K_s band drives the color index redward for later types. The redward trend of the $K_s - [3.6]$ color index turns blueward as the fundamental CH_4 absorption feature at 3.2 μm switches on at mid-L, and then turns redward again at mid-T when this feature saturates and 2.2 μm CH_4 absorption and CIA H_2 in the K_s band assert themselves at mid-T.

These color versus spectral-type plots serve to show that in the previously presented color-color diagrams based on IRAC photometry alone, much of the scatter in the T dwarf colors comes from the $[4.5] - [5.8]$ and $[5.8] - [8.0]$ color indices. The trending of color versus spectral type for the $[3.6] - [4.5]$ color index is very smooth. While some of the scatter in the $[5.8] - [8.0]$ color index could be due to the interplay of H_2O absorption (starting in the $\sim$late M types) versus the 7.7 μm overtone band of CH_4 in the IRAC 8.0 μm filter (beginning at $\sim$mid-L types), it is also true that our fixed integration time AORs yield the highest quality data for IRAC channels 1 and 2, the most sensitive of the four IRAC channels, and thus systematically lower S/N data for our sample in IRAC channels 3 and 4 (i.e., some of the scatter seen in $[5.8] - [8.0]$ might be due to the larger errors on this color index compared to the others presented in Fig. 10).

5. DISCUSSION

As shown in the previous sections, the infrared colors of low-mass stars and brown dwarfs are generally well correlated with their spectral types. In turn, the spectral types of M, L, and T dwarfs
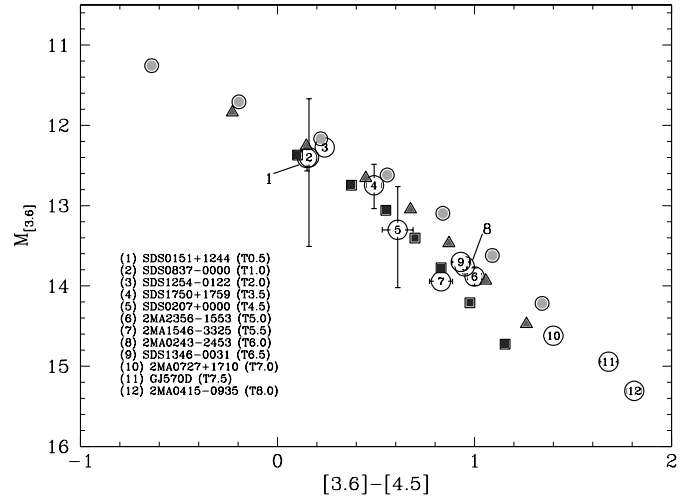

Fig. 11.—Color-magnitude diagram of $M_{3.6}$ vs. the $[3.6] - [4.5]$ color for the T dwarfs in our program, with trigonometric parallaxes. As in the previous figures in this paper, known binaries and spectrally peculiar objects have been excluded. Each T dwarf plotted is numbered 1 to 12 in order of increasing spectral subtype. The accompanying error bars include the estimated photometric errors and the published errors in the distance estimates for each individual object (in some cases, the error bars are smaller than the plot symbol). The squares are models for T_{eff} from 1300 to 700 K (left to right, in steps of 100 K) at $g = 10^{5.5}$ cm s^{-2}, the triangles and circles are models for the same temperature range as at $g = 10^5$ cm s^{-2} and $g = 10^{4.5}$ cm s^{-2}, respectively. The corresponding masses range from $\sim 15 M_J$ to $70 M_J$ (Burrows et al. 1997). [See the electronic edition of the Journal for a color version of this figure.]

are reasonably well correlated with their effective temperatures, although to a lesser degree than for higher mass objects because molecular chemistry and particulate clouds compete aggressively in determining the detailed spectral energy distributions of cool dwarfs. Theoretical models are beginning to be able to match the observed spectral properties of very cool dwarfs, and we have used those models to help interpret the IRAC photometry in § 4.

While a detailed theoretical analysis of these new Spitzer IRAC data is beyond the scope of this paper, there are a few conclusions of a general nature that can be extracted at this preliminary
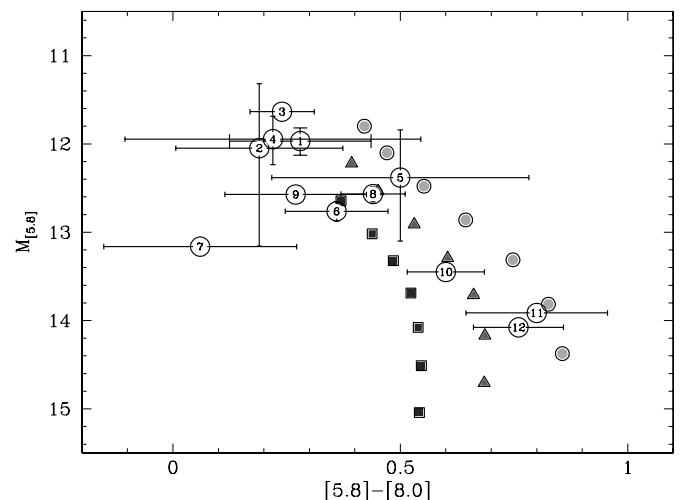

Fig. 12.—Color-magnitude diagram of $M_{5.8}$ vs. the $[5.8] - [8.0]$ color. Otherwise, the format is the same as in Fig. 11. The theoretical models are also the same and span T_{eff} from 1300 to 700 K, in steps of 100 K, for gravities of $10^{5.5}$ cm s^{-2} (squares), 10^5 cm s^{-2} (triangles), and $10^{4.5}$ cm s^{-2} (circles). [See the electronic edition of the Journal for a color version of this figure.]
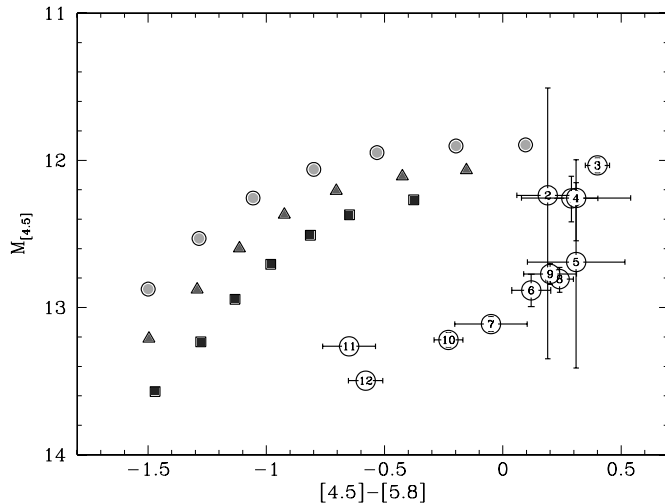
FIG. 13.—Color-magnitude diagram of $M_{4.5}$ vs. the [4.5]−[5.8] color. Otherwise, the format is the same as in Fig. 11. For this color-magnitude diagram, the theoretical fits (the same as in Fig. 11) are unacceptable. Because CO has a strong spectral feature at ∼4.67 μm, one can interpret the discrepancy between theory and the IRAC data as an indication that equilibrium CH_4/CO chemistry underestimates the abundance of CO in T dwarf atmospheres (Golimowski et al. 2004a). The magnitude of the discrepancy translates into an overestimate in the ∼4−5 μm flux by factors of 1.5−3.0. [See the electronic edition of the Journal for a color version of this figure.]

FIG. 14.—Comparison between a theoretical T dwarf spectral model with $T_{\rm eff}/g = 750$ K/10^5 cm s^{-2} and the IRAC fluxes measured for the T7.5 dwarf GJ 570D. A distance of 5.89 pc has been assumed (Dahn et al. 2002). The triangles depict the fluxes (with their uncertainties) derived from the IRAC photometry; the horizontal lines indicate the widths of the IRAC bands. This model was generated for GJ 570D in 2002 to fit its optical spectrum shortward of 1.0 μm (Burrows et al. 2002). No further attempt was made to improve the fit. A slight (∼40%) discrepancy in the 4.5 μm bandpass, attributable to a CO abundance excess in the atmosphere, is manifest. Despite this, this plot and Fig. 7 in Burrows et al. (2002) represent a good fit (that can nevertheless be improved) from 0.6 μm to ∼8.0 μm and indicate that the IRAC data were successfully anticipated. [See the electronic edition of the Journal for a color version of this figure.]

stage. To do so, we have generated three color-magnitude plots (Figs. 11–13) for most of the T dwarfs in our sample, with parallaxes and superposed synthetic magnitudes and colors derived from theoretical spectra for an effective temperature ($T_{\rm eff}$) range from 700 to 1300 K, in steps of 100 K at three gravities. These gravities are $10^{4.5}$ cm s^{-2} (circles), 10^5 cm s^{-2} (triangles), and $10^{5.5}$ cm s^{-2} (squares). Figure 11 depicts the absolute magnitude in the IRAC 3.6 μm bandpass versus the [3.6]−[4.5] color. The legend on this figure indicates the T dwarfs included in this figure, and they are numbered in order of spectral subtype.

As Figure 11 demonstrates, despite the fact that the numbering is in order of increasing spectral subtype, the 3.6 μm IRAC data are not monotonic in either magnitude or color. That they are not in order in magnitude may in part be ascribed to multiplicity. However, this cannot be the explanation for the majority of these T dwarfs. Furthermore, the [3.6]−[4.5] colors, too, are nonmonotonic in spectral type. This is even more obvious in Figure 12, which portrays $M_{5.8}$ versus [5.8]−[8.0]. For example, SDS 1346−0031 and 2MA 0727+1710 only differ by half a spectral subtype, but they have very different colors.

The nonmonotonicity of these Spitzer IRAC data is the clearest indication yet that the T dwarfs are not a one-parameter family in $T_{\rm eff}$, but that more than one parameter is influential in determining the spectroscopic type. Because the metallicity cannot generically vary enough in the solar neighborhood to explain this, the extra parameter may be gravity. This was the conclusion of Burrows et al. (2002) and Knapp et al. (2004) using different data sets at shorter wavelengths, and is confirmed here. For the T dwarfs, gravity will translate into mass (Burrows et al. 1997). From the comparison of the spread in the data in Figures 11 and 12 with the spread with gravity of the theoretical models, we conclude that a range of gravities of approximately a factor of 5 is represented in the extant T dwarf sample. This can be converted into a range of masses from ∼$70M_J$ to ∼$15M_J$. The less massive objects would also be younger, and a range of ages of about a factor
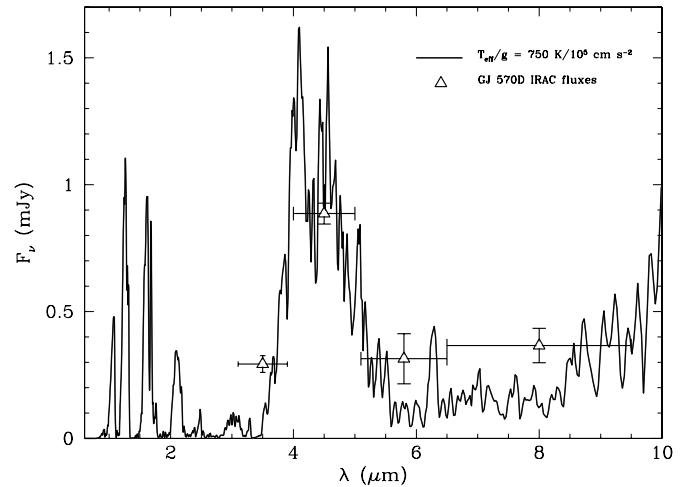
of 10 (0.2–0.3 to 10 Gyr) is indicated (Burrows et al. 1997, 2001). The latter conclusion might be problematic, but such is indicated by our preliminary analysis.

Figure 13 is an H-R diagram of IRAC $M_{4.5}$ versus the IRAC [4.5]−[5.8] color. The nonmonotonicity of the data seen in previous plots' color survives in this plot as well. However, as is abundantly clear in the figure, the theoretical models do not fit these data. Because CO has a strong spectral feature at ∼4.67 μm, one can interpret the discrepancy between theory and the IRAC data as an indication that equilibrium CH_4/CO chemistry underestimates the abundance of CO in T dwarf atmospheres. This conclusion was already reached by Golimowski et al. (2004a) using M-band measurements from the ground. The magnitude of the discrepancy translates into an overestimate in the ∼4−5 μm flux by factors of 1.5−3.0.

It should be noted that the opacities of water in the mid-infrared are still being studied and refined (Schwenke 2002). Continuing ambiguity in the H_2O opacities is a source of systematic theoretical error, with the product of the O abundance and the H_2O opacity directly connected to the goodness of fit at 5.8 and 8.0 μm for the later T dwarfs. Moreover, at the lowest $T_{\rm eff}$ represented here, the condensation of K into KCl and Na into Na_2S could introduce hazes with interesting optical depths. Finally, the early T dwarf spectra show signs of silicate clouds (Stephens et al. 2001; Marley et al. 2002; Burrows et al. 2002) not included in the models we have presented. Hence, the study of substellar mass object atmospheres is still in its formative years.

Nevertheless, as Figure 14 implies, one can be encouraged that the basics are falling into place. Figure 14 compares a theoretical T dwarf spectral model with $T_{\rm eff}/g = 750$ K/10^5 cm s^{-2} (Burrows et al. 2002; Geballe et al. 2001) with the four IRAC fluxes measured for the T7.5 dwarf GJ 570D. This model was generated in 2002 for GJ 570D to fit its optical spectrum shortward of 1.0 μm (Burrows et al. 2002). A slight (∼40%) discrepancy in the

4.5 μm bandpass, attributable to a CO abundance excess in its atmosphere, is visible. Despite this, Figure 14 from this paper and Figure 7 in the related paper by Burrows et al. (2002) together represent an acceptable fit from 0.6 to ~8.0 μm and indicate that the IRAC data were successfully anticipated.

REFERENCES

Ackerman, A. S., & Marley, M. S. 2001, ApJ, 556, 872
Allard, F., Hauschildt, P. H., Alexander, D. R., Tamanai, A., & Schweitzer, A. 2001, ApJ, 556, 357
Allard, F., Hauschildt, P. H., Miller, S., & Tennyson, J. 1994, ApJ, 426, L39
Bailer-Jones, C. A. L. 2004, A&A, 419, 703
Basri, G., et al. 2000, ApJ, 538, 363
Becklin, E., & Zuckerman, B. 1988, Nature, 336, 656
Bessell, M. S. 1991, AJ, 101, 662
Bessell, M. S., & Brett, J. M. 1988, PASP, 100, 1134
Bloom, J. S., Starr, D. L., Blake, C. H., Skrutskie, M. F., & Falco, E. E. 2006, in ASP Conf. Ser. 351, Astronomical Data Analysis Software and Systems XV, ed. C. Gabriel et al. (San Francisco: ASP), 751
Bouy, H., et al. 2004, A&A, 423, 341
Brett, J. M. 1995, A&A, 295, 736
Burgasser, A. J., Geballe, T. R., Leggett, S. K., Kirkpatrick, J. D., & Golimowski, D. A. 2006a, ApJ, 637, 1067
Burgasser, A. J., Kirkpatrick, J. D., Liebert, J., & Burrows, A. 2003a, ApJ, 594, 510
Burgasser, A. J., Kirkpatrick, J. D., & Lowrance, P. J. 2005a, AJ, 129, 2849
Burgasser, A. J., Reid, I. N., Leggett, S. K., Kirkpatrick, J. D., Liebert, J., & Burrows, A. 2005b, ApJ, 634, L177
Burgasser, A. J., et al. 2002, ApJ, 564, 421
———. 2003b, ApJ, 592, 1186
———. 2006b, ApJ, 639, 1095
Burrows, A., Burgasser, A. J., Kirkpatrick, J. D., Liebert, J., Milsom, J. A., Sudarsky, D., & Hubeny, I. 2002, ApJ, 573, 394
Burrows, A., Hubbard, W. B., Lunine, J. I., & Liebert, J. 2001, Rev. Mod. Phys., 73, 719
Burrows, A., Marley, M. S., & Sharp, C. M. 2000, ApJ, 531, 438
Burrows, A., et al. 1997, ApJ, 491, 856
Close, L., et al. 2005, Nature, 433, 286
Cohen, M. 2003, in Proc. The Calibration Legacy of the *ISO* Mission, ed. L. Metcalfe et al. (ESA SP-481; Noordwijk: ESA), 135
Cohen, M., Megeath, S. T., Hammersley, P. L., Martín-Luis, F., & Stauffer, J. 2003, AJ, 125, 2645
Costa, E., et al. 2005, AJ, 130, 337
Cruz, K. L., Reid, I. N., Liebert, J., Kirkpatrick, J. D., & Lowrance, P. J. 2003, AJ, 126, 2421
Cushing, M. C., Rayner, J. T., & Vacca, W. D. 2005, ApJ, 623, 1115
Dahn, C. C., et al. 2002, AJ, 124, 1170
Fan, X., et al. 2000, AJ, 119, 928
Fazio, G. G., et al. 2004, ApJS, 154, 10
Geballe, T. R., Saumon, D., Leggett, S. K., Knapp, G. R., Marley, M. S., & Lodders, K. 2001, ApJ, 556, 373
Geballe, T. R., et al. 2002, ApJ, 564, 466
Gelino, C. R. 2002, Ph.D. thesis, New Mexico State Univ.
Gizis, J. E. 2002, ApJ, 575, 484
Gizis, J. E., Monet, D. G., Reid, I. N., Kirkpatrick, J. D., Liebert, J., & Williams, R. J. 2000, AJ, 120, 1085
Gizis, J. E., Reid, I. N., Knapp, G. R., Liebert, J., Kirkpatrick, J. D., Koerner, D. W., & Burgasser, A. J. 2003, AJ, 125, 3302
Golimowski, D. A., et al. 2004a, AJ, 127, 3516
———. 2004b, AJ, 128, 1733
Gould, A., & Chaname, J. 2004, ApJS, 150, 455

Grossman, A. S. 1970, ApJ, 161, 619
Hawley, S. L., et al. 2002, AJ, 123, 3409
Henry, T. J., Kirpatrick, J. D., & Simons, D. A. 1994, AJ, 108, 1437
Henry, T. J., & McCarthy, D. 1993, AJ, 106, 773
Henry, T. J., Subasavage, J. P., Brown, M. A., Beaulieu, T. D., Jao, W.-C., & Hambly, N. C. 2004, AJ, 128, 2460
Henry, T. J., et al. 1999, ApJ, 512, 864
Kirkpatrick, J. D. 2005, ARA&A, 43, 195
Kirkpatrick, J. D., Henry, T. J., & Irwin, M. J. 1997, AJ, 113, 1421
Kirkpatrick, J. D., Henry, T. J., McCarthy, D. W., Jr. 1991, ApJS, 77, 417
Kirkpatrick, J. D., Henry, T. J., & Simons, D. A. 1995, AJ, 109, 797
Kirkpatrick, J. D., et al. 1999, ApJ, 519, 802
———. 2000, AJ, 120, 447
———. 2001, AJ, 121, 3235
Knapp, G. R., et al. 2004, AJ, 127, 3553
Koen, C. 2004, MNRAS, 354, 378
———. 2005, MNRAS, 360, 1132
Kumar, S. S. 1963, ApJ, 137, 1121
Lane, B. F., Zapatero Osorio, M. R., Britton, M. C., Martín, E. L., & Kulkarni, S. R. 2001, ApJ, 560, 390
Leggett, S. K. 1992, ApJS, 82, 351
Leggett, S. K., Allard, F., Geballe, T. R., Hauschildt, P. H., & Schweitzer, A. 2001, ApJ, 548, 908
Leggett, S. K., et al. 2000, ApJ, 536, L35
———. 2002, ApJ, 564, 452
Liu, M. C., & Leggett, S. K. 2005, ApJ, 634, 616
Lodders, K., & Fegley, B. 2002, Icarus, 155, 393
Marley, M. S., et al. 2002, ApJ, 568, 335
Martín, E. L., Zapatero Osorio, M. R., & Lehto, H. J. 2001, ApJ, 557, 822
Mohanty, S., & Basri, G. 2003, ApJ, 583, 451
Nakajima, T., Oppenheimer, B. R., Kulkarni, S. R., Golimowski, D. A., Matthews, K., & Durrance, S. T. 1995, Nature, 378, 463
Nelson, L. A., Rappaport, S. A., & Joss, P. C. 1985, Nature, 316, 42
Noll, K. S., Geballe, T. R., & Marley, M. S. 1997, ApJ, 489, L87
Perryman, M. A. C., et al. 1997, A&A, 323, L49
Reach, W. T., et al. 2005, PASP, 117, 978
Reid, I. N., & Gizis, J. E. 2005, PASP, 117, 676
Reid, I. N., Gizis, J. E., Kirkpatrick, J. D., & Koerner, D. W. 2001, AJ, 121, 489
Reid, I. N., Kirkpatrick, J. D., Liebert, J., Gizis, J. E., Dahn, C. C., & Monet, D. G. 2002, AJ, 124, 519
Reid, I. N., et al. 2000, AJ, 119, 369
———. 2003, AJ, 125, 354
Reiners, A., & Basri, G. 2006, AJ, 131, 1806
Ribas, I. 2003, A&A, 400, 297
Saumon, D., Marley, M. S., Lodders, K., & Freedman, R. S. 2003, in IAU Symp. 211, Brown Dwarfs, ed. E. L. Martin (San Francisco: ASP), 345
Saumon, D., et al. 2000, ApJ, 541, 374
———. 2006, ApJ, 647, 552
Scholz, R.-D., Irwin, M., Ibata, R., Jahreiss, H., & Malkov, O. Y. 2000, A&A, 353, 958
Schuster, M. T., Marengo, M., & Patten, B. M. 2006, Proc. SPIE, 6270, 627020
Schwenke, D. W. 2002, AGU Abstr. Fall, SA71A-10
Stephens, D. C., & Leggett, S. K. 2004, PASP, 116, 9

Stephens, D., Marley, M. S., & Noll, K. 2001, in Ultracool Dwarfs: New Spectral Types L and T, ed. H. R. A. Jones & I. A. Steele (Berlin: Springer), 183
Tinney, C. G. 1998, MNRAS, 296, L42
Tinney, C. G., Burgasser, A. J., & Kirkpatrick, J. D. 2003, AJ, 126, 975
Tinney, C. G., & Reid, I. N. 1998, MNRAS, 301, 1031
Tokunaga, A. T., Simons, D. A., & Vacca, W. D. 2002, PASP, 114, 180
Tsuji, T. 2002, ApJ, 575, 264

Vrba, F. J., et al. 2004, AJ, 127, 2948
Wilson, J. C., Kirkpatrick, J. D., Gizis, J. E., Skrutskie, M. F., Monet, D. G., & Houck, J. R. 2001, AJ, 122, 1989
Wilson, J. C., et al. 2003, in IAU Symp. 211, Brown Dwarfs, ed. E. L. Martin (San Francisco: ASP), 197
Zapatero Osorio, M. R., Lane, B. F., Pavlenko, Y., Martín, E. L., Britton, M., & Kulkarni, S. R. 2004, ApJ, 615, 958